THE EARLY UV/OPTICAL EMISSION FROM CORE-COLLAPSE SUPERNOVAE

ITAY RABINAK AND ELI WAXMAN
Department of Particle Physics and Astrophysics, The Weizmann Institute of Science, Rehovot 76100, Israel; itay.rabinak@weizmann.ac.il

ABSTRACT

We derive a simple approximate model describing the early, hours to days, UV/optical (UV/O) supernova emission, which is produced by the expansion of the outer $\lesssim 10^{-2}\, M_\odot$ part of the shock-heated envelope, and precedes optical emission driven by radioactive decay. Our model includes an approximate description of the time dependence of the opacity (mainly due to recombination), and of the deviation of the emitted spectrum from a blackbody spectrum. We show that the characteristics of the early UV/O emission constrain the radius of the progenitor star, R_*, its envelope composition, and the ratio of the ejecta energy to its mass, E/M. For He envelopes, neglecting the effect of recombination may lead to an overestimate of R_* by more than an order of magnitude. We also show that the relative extinction at different wavelengths ($A_\lambda - A_V$) may be inferred from the light curves at these wavelengths, removing the uncertainty in the estimate of R_* due to reddening (but not the uncertainty in E/M due to uncertainty in absolute extinction). The early UV/O observations of the types Ib SN 2008D and IIp SNLS−04D2dc are consistent with our model predictions. For SN 2008D, we find $R_* \approx 10^{11}$ cm, and an indication that the He envelope contains a significant C/O fraction.

Key words: radiative transfer – shock waves – stars: evolution – supernovae: general – supernovae: individual (SN 2008D)

Online-only material: color figures

1. INTRODUCTION

Over the past four years, the wide-field X-ray detectors on board the *Swift* satellite enabled us, for the first time, to "catch" supernova (SN) explosions very close to the onset of the explosion. In two cases, SN2006aj and SN 2008D, the usual optical SN light curve was observed to be preceded by a luminous X-ray outburst, which has triggered the X-ray detectors, followed by a longer, ∼1 day, duration UV/optical (UV/O) emission (Campana et al. 2006; Soderberg et al. 2008). Analysis of the later optical SN emission revealed that both were of type Ib/c, probably produced by compact Wolf–Rayet (hereafter WR) progenitor stars, which lost most of their hydrogen envelope (Pian et al. 2006; Mazzali et al. 2006, 2008; Modjaz et al. 2006; Maeda et al. 2007; Malesani et al. 2009). Following the detection of the early UV/O emission from these SNe, a search was conducted for UV/O emission from SNe that fall within the deep imaging survey of the *Galaxy Evolution Explorer* (*GALEX*) space telescope, leading to the detection of early (∼1 day) rising UV/O emission for two type II-p SNe (Gezari et al. 2008; Schawinski et al. 2008), for which the progenitors are likely red super giants (hereafter RSGs) with large hydrogen envelopes.

X-ray outbursts followed by early UV emission have long been expected to mark the onset of SN explosions. The SN shock wave, which travels through and ejects the stellar envelope, becomes radiation mediated when propagating through the envelope (for review see, e.g., Woosley & Weaver 1986). As the shock propagates outward, the (Thomson) optical depth of the plasma lying ahead of it decreases. When this optical depth becomes comparable to the shock transition optical depth, $\tau_s \simeq c/v_s$ (v_s is the shock velocity), the radiation escapes ahead of the shock. This leads to an expected "shock breakout" X-ray flash (Colgate 1974; Falk 1978; Klein & Chevalier 1978) lasting for tens to hundreds of seconds. Following breakout, the stellar envelope expands and cools (nearly adiabatically). As

the photosphere penetrates into the outer shells of the envelope, the (adiabatically cooled) radiation stored within the envelope escapes, leading to an expected early UV/O emission (Falk 1978). In this paper, we focus on the early, ∼1 day, part of this UV/O emission (although it may dominate the total emission for much longer, e.g., in type II-P SNe).

The interpretation of SN associated X-ray outbursts as due to "shock breakout" is not generally accepted, due mainly to the fact that while a ∼0.1 keV thermal spectrum was expected, the observed spectra are non-thermal and extend beyond 10 keV. Some authors (Campana et al. 2006; Waxman et al. 2007; Soderberg et al. 2008) argued that this is due to shock breakout physics. Others argued that the X-ray bursts cannot be explained within this framework and imply the existence of relativistic energetic jets penetrating through the stellar mantle/envelope (Soderberg et al. 2006; Fan et al. 2006; Ghisellini et al. 2007; Li 2007; Mazzali et al. 2008; Li 2008). A recent derivation of the structure of mildly and highly relativistic radiation-mediated shocks (Katz et al. 2010) shows that fast, $v_s/c \gtrsim 0.2$, radiation mediated shocks produce photons of energy far exceeding the ∼0.1 keV downstream temperature, reaching tens to hundreds of keV. This suggests that the observed outbursts may indeed be due to shock breakout. (Note that for SN2006aj, there is an additional challenge, beyond the X-ray spectrum: the energy inferred to be deposited in the fastest part of the ejecta far exceeds that expected from shock acceleration in the envelope.)

Our focus in this paper is not on the X-ray outburst, but rather on the early, ∼1 day, UV/O emission that follows it. Model predictions for the early UV/O emission were derived mainly using numerical calculations (e.g., Falk 1978; Ensman & Burrows 1992; Blinnikov et al. 2000, 2002; Gezari et al. 2008). Following the detection of SN2006aj, an analytic model has been constructed (Waxman et al. 2007). One of the main advantages of the analytic model is that it provides explicit analytic expressions for the dependence of the emission on model parameters, thus making both the use of observations

for determining parameters and the identification of model uncertainties much easier and more straightforward. It was shown, in particular, that the photospheric temperature of the expanding envelope depends mainly on the progenitor's radius and on the opacity, T_{ph} approximately proportional to $R_*^{1/4}$, and that the luminosity L is approximately proportional to $(E/M)R_*$. This implies that the progenitor radius, which is only poorly constrained by other observations, and E/M may be directly determined by measuring and analyzing the early UV/O emission.

In should be noted here that most numerical models, which are used for analyzing SN light curves, focus on the long-term radioactively driven emission. Such models do not describe the early UV/O emission (e.g., Figure 3 in Tanaka et al. 2009), largely due to the fact that they lack the resolution required to properly describe the evolution of the outer $\sim 10^{-2} M_\odot$ part of the shock-heated envelope, which drives the early emission (Waxman et al. 2007). Numerical calculations that allow a proper treatment of the early emission are, on the other hand, computationally very demanding (see, e.g., Gezari et al. 2008; Blinnikov et al. 2000). It is difficult to use these models for obtaining the dependence of predictions on model parameters and therefore for using observations to constrain these parameters.

In the near future, we expect an increasing rate of detection of early UV/O SN emission. Ground-based SN surveys with high rate sampling (less or order of a day, e.g., Law et al. 2009; Quimby 2006) will detect SNe at the early stages of their expansion, with a bias toward detection of the more abundant type II SNe. The detection of X-ray outbursts, that were observed to mark the onset of several SN Ib/c explosions, suggest that the early UV/O emission from these SNe may be detectable by follow-ups of X-ray triggers. The Monitor of All-sky X-ray Image (MAXI) experiment on board the Kibo module (Matsuoka et al. 1997), which was launched this year, is expected to detect events similar to SN 2008D at a rate of up to a few per year. The *EXIST* satellite (Grindlay et al. 2003; Band et al. 2008), which is still in planning, will further increase the event rate and improve the X-ray spectral coverage. (The detection rate may also be enhanced by smaller dedicated X-ray observatories, see, e.g., Calzavara & Matzner 2004.)

The main goal of this paper is to extend the analytic model (Waxman et al. 2007) to include a more realistic description of the opacity and its variation with time (mainly due to recombination), and to include an approximate description of the deviation of the emitted spectrum from a blackbody spectrum (due to photon diffusion). Our results will facilitate the use of upcoming observations of the early emission from SNe for constraining progenitor and explosion parameters. We consider several types of progenitor envelopes: dominated by hydrogen, as appropriate for RSG and blue super giant (BSG) progenitors, as well as envelopes dominated by He, C/O, and He-C/O mixtures representing different degrees of H/He stripping, due to wind mass loss (e.g., Woosley et al. 1993) or binary interaction (e.g., Nomoto et al. 1995), and different evolution scenarios (e.g., due to rotation induced mixing, Meynet & Maeder 2003; Crowther 2007).

For completeness, we first present in Section 2 the simple model derived in Waxman et al. (2007). The main assumptions adopted are that the envelope density drops near the stellar edge as a power of the distance from the edge, Equation (1), that the SN shock velocity may be approximated (following Matzner & McKee 1999) by an interpolation between

the Sedov–von Neumann–Taylor and the Gandel'Man–Frank-Kamenetskii–Sakurai self-similar solutions, Equation (2), and that the opacity, κ, is space and time independent. We also show, in Section 2.3, that the effects of photon diffusion on the predicted luminosity (considered in Chevalier 1992; Chevalier & Fransson 2008) are small. The model is extended in Section 3 to include a more realistic description of the opacity and an approximate description of the effect of photon diffusion on the spectrum. In Section 4, we show that the relative extinction at different wavelengths ($A_\lambda - A_V$) may be inferred from the light curves at these wavelengths. In Section 5, we compare our model predictions to observations of the early emission available for two SNe, arising from RSG and BSG progenitors, and to detailed numerical simulations that were constructed to reproduce these observations. In Section 6, we use our model to analyze the early UV/O observations of SN 2008D. Our main results are summarized and discussed in Section 7.

2. A SIMPLE MODEL

We first derive in Section 2.1 the density, velocity, and temperature profiles of the (post-breakout) expanding stellar envelope. We then derive in Section 2.2 the radius and temperature of the photosphere. These derivations are carried out under the simplifying assumption that photon diffusion is negligible (and hence that the flow is adiabatic) below the photosphere. This assumption is justified in Section 2.3.

2.1. Expanding Ejecta Profiles

The UV/O emission on a day timescale arises from the outer $\lesssim 10^{-2} M_\odot$ shell of the ejecta (Waxman et al. 2007). Neglecting the shell's self-gravity and its thickness (relative to R_*), the pre-explosion density profile within the shell may be approximated by Chandrasekhar (1939):

$$\rho_0(r_0) = \rho_{1/2}\delta^n, \tag{1}$$

where $\delta \equiv (1 - r_0/R_*)$, r_0 is the radius, and $n = 3, 3/2$ for radiative and efficiently convective envelopes, respectively. Matzner & McKee (1999) have shown that the velocity of the SN shock within the envelope is well approximated by an interpolation between the Sedov–von Neumann–Taylor and the Gandel'Man–Frank-Kamenetskii–Sakurai self-similar solutions, (Von Neumann 1947; Sedov 1959; Taylor 1950; Gandel'Man & Frank-Kamenetskii 1956; Sakurai 1960):

$$v_s(r_0) = A_v \left[\frac{E}{m(r_0)}\right]^{1/2} \left[\frac{m(r_0)}{\rho r_0^3}\right]^{\beta_1}, \tag{2}$$

where E is the energy deposited in the ejecta, $m(r_0)$ is the ejecta mass enclosed within r_0, $A_v \simeq 0.79$, and $\beta_1 \simeq 0.19$. For $r_0 \to R_*$, Equation (2) reduces to

$$v_s \simeq A_v \left(\frac{E}{M}\right)^{1/2} \left(\frac{4\pi}{3f_\rho}\right)^{\beta_1} \delta^{-\beta_1 n}, \tag{3}$$

where $f_\rho \equiv \rho_{1/2}/\overline{\rho}_0$, and $\overline{\rho}_0$ is the average ejecta density, $\overline{\rho}_0 \equiv 3M/4\pi R_*^3$. Calzavara & Matzner (2004, Appendix A) have derived the values of f_ρ expected for various progenitors (using their notation, $f_\rho = (3/4\pi)\rho_1/\rho_*$). For BSGs, they find f_ρ varying nearly linearly with mass, from 0.031 to 0.062 for $8.5 < M/M_\odot < 18.5$, and for RSGs, they find $0.079 \lesssim f_\rho \lesssim 0.13$. We show below that the results are not very sensitive to the value of f_ρ.

In what follows, we replace the Lagrangian coordinate r_0 with

$$\delta_m(\delta) \equiv M^{-1} \int_{(1-\delta)R_*}^{R_*} dr 4\pi r^2 \rho_0(r) \simeq \frac{3 f_\rho}{n+1} \delta^{n+1}, \qquad (4)$$

the fraction of the ejecta mass lying initially above r_0.

As the radiation mediated shock passes through a fluid element lying at r_0, it increases its pressure to

$$p_0 = \frac{6}{7} \rho_0 v_s^2, \qquad (5)$$

and its density to $7\rho_0$. (Recall that the post-shock energy density is dominated by radiation.) As the shocked fluid expands, it accelerates, converting its internal energy to kinetic energy. Matzner & McKee (1999) have shown that the final velocity, $v_f(r_0)$, of the fluid initially lying at r_0 is well approximated by $v_f(r_0) = f_v(r_0) v_s(r_0)$, with $f_v \approx 2$. The value of f_v depends on the curvature of the shells. The effect of this dependence is considered below.

Equations (3) and (5) hold as long as the shock width is much smaller than the width of the stellar envelope shell lying ahead of the shock. When the shock reaches a radius at which the optical depth of the shock transition layer, $\tau_s \cong c/v_s$, becomes comparable to the optical depth of the shell lying ahead of the shock, $\tau_0 \simeq M\delta_m \kappa/4\pi R_*^2$, the radiation "escapes" ahead of the shock, producing a "shock breakout flash," and the shock can no longer be sustained by radiation. The mass fraction at which breakout takes place is (e.g., Matzner & McKee 1999)

$$\delta_{m,\text{BO}} \simeq 2 \times 10^{-5} \frac{f_\rho^{-0.07} R_{*,13}^{2.3}}{E_{51}^{0.57} (M/M_\odot)^{0.57} \kappa_{0.34}^{1.1}}. \qquad (6)$$

For smaller values of δ_m, $\delta_m < \delta_{m,\text{BO}}$, the velocity and pressure profiles are shallower than given by Equations (3) and (5).

Assuming adiabatic expansion, neglecting photon diffusion below the photosphere, the pressure and density of the expanding fluid are related by

$$p(\delta_m, t) = \left[\frac{\rho(\delta_m, t)}{7\rho_0(\delta_m)} \right]^{4/3} p_0(\delta_m). \qquad (7)$$

Once a fluid shell expands to a radius significantly larger than R_*, its pressure drops well below p_0 and its velocity approaches the final velocity v_f. At this stage, $v_f t \gg R_*$, the shell's radius is approximately given by

$$r(\delta_m, t) \cong v_f(\delta_m) t, \qquad (8)$$

and its density is then given by

$$\rho = -\frac{M}{4\pi r^2 t} \left(\frac{dv_f}{d\delta_m} \right)^{-1} \cong \frac{n+1}{\beta_1 n} \frac{M}{4\pi t^3 v_f^3} \delta_m. \qquad (9)$$

The resulting density profile is steep, $d \ln \rho / d \ln r = d \ln \rho / d \ln v_f = -3 - (n+1)/\beta_1 n \approx -10$.

2.2. Photospheric Temperature and Radius

For a time- and space-independent opacity κ (which applies, e.g., for opacity dominated by Thomson scattering with constant ionization), the optical depth of the plasma lying above the shell

marked by δ_m is

$$\tau(\delta_m, t) \equiv \int_{r(\delta_m, t)}^{\infty} dr \kappa \rho(r, t) = \frac{\kappa M}{4\pi} \int_0^{\delta_m} \frac{d\delta_m'}{r^2(\delta_m')}$$
$$= \frac{1}{1 + 2\beta_1 n/(1+n)} \frac{\kappa M \delta_m}{4\pi t^2 v_f^2(\delta_m)}, \qquad (10)$$

where the last equality holds when Equation (8) is satisfied. We define the Lagrangian location of the photosphere, $\delta_{m,\text{ph}}$, by $\tau(\delta_m = \delta_{m,\text{ph}}, t) = 1$. We consider two type of envelopes: radiative envelopes typical to BSGs, for which we take $n = 3$, and efficiently convective envelopes typical to RSGs, for which we take $n = 3/2$. (Note that inefficient convection may lead to a more complicated density profile.) For $n = 3/2$ and $n = 3$ envelopes, we have

$$\delta_{m,\text{ph}}(t) = 2.4 \times 10^{-3} f_\rho^{-0.12} \frac{E_{51}^{0.81}}{(M/M_\odot)^{1.6} \kappa_{0.34}^{0.81}} t_5^{1.63} \left(n = \frac{3}{2} \right),$$

$$\delta_{m,\text{ph}}(t) = 2.6 \times 10^{-3} f_\rho^{-0.073} \frac{E_{51}^{0.78}}{(M/M_\odot)^{1.6} \kappa_{0.34}^{0.78}} t_5^{1.56} (n = 3), \qquad (11)$$

where $E = 10^{51} E_{51}$ erg, $t = 10^5 t_5$ s, and $\kappa = 0.34\kappa_{0.34}$ cm^2 g^{-1}. Here, and in what follows, we use (following Matzner & McKee 1999) $\beta_1 = 0.1909$, $f_v = 2.1649$, and $A_v = 0.7921$ for $n = 3/2$ and $\beta_1 = 0.1858$, $f_v = 2.0351$, and $A_v = 0.8046$ for $n = 3$. Using Equations (3), (8), and (7), we find that the radius and the effective temperature of the photosphere are given by

$$r_{\text{ph}}(t) = 3.3 \times 10^{14} f_\rho^{-0.062} \frac{E_{51}^{0.41} \kappa_{0.34}^{0.093}}{(M/M_\odot)^{0.31}} t_5^{0.81} \text{ cm} \left(n = \frac{3}{2} \right),$$

$$r_{\text{ph}}(t) = 3.3 \times 10^{14} f_\rho^{-0.036} \frac{E_{51}^{0.39} \kappa_{0.34}^{0.11}}{(M/M_\odot)^{0.28}} t_5^{0.78} \text{ cm} (n = 3), \qquad (12)$$

and

$$T_{\text{ph}}(t) = 1.6 f_\rho^{-0.037} \frac{E_{51}^{0.027} R_{*,13}^{1/4}}{(M/M_\odot)^{0.054} \kappa_{0.34}^{0.28}} t_5^{-0.45} \text{ eV} \left(n = \frac{3}{2} \right),$$

$$T_{\text{ph}}(t) = 1.6 f_\rho^{-0.022} \frac{E_{51}^{0.016} R_{*,13}^{1/4}}{(M/M_\odot)^{0.033} \kappa_{0.34}^{0.27}} t_5^{-0.47} \text{ eV} (n = 3). \qquad (13)$$

Here, $R_* = 10^{13} R_{*,13}$ cm. The dependence on n and on f_ρ is weak. Note that Equation (13) corrects a typo (in the numerical coefficient) in Equation (19) of Waxman et al. (2007).

As mentioned in the introduction, the photospheric temperature is weakly dependent on E and M and is approximately linear in $(R_*/\kappa)^{1/4}$. The photospheric radius, on the other hand, does not depend on R_*, is weakly dependent on κ and is approximately linear in $E^{0.4}/M^{0.3}$. The luminosity predicted by the simple model described here, $L = 4\pi \sigma r_{\text{ph}}^2 T_{\text{ph}}^4$, is

$$L = 8.5 \times 10^{42} \frac{E_{51}^{0.92} R_{*,13}}{f_\rho^{0.27} (M/M_\odot)^{0.84} \kappa_{0.34}^{0.92}} t_5^{-0.16} \text{ erg s}^{-1} \qquad (14)$$

for $n = 3/2$, and

$$L = 9.9 \times 10^{42} \frac{E_{51}^{0.85} R_{*,13}}{f_\rho^{0.16} (M/M_\odot)^{0.69} \kappa_{0.34}^{0.85}} t_5^{-0.35} \text{ erg s}^{-1} \qquad (15)$$

for $n = 3$.

Our simple description of $r_{\rm ph}$, $T_{\rm ph}$, and L, Equations (12)–(15), holds for $\delta_{m,\rm ph} > \delta_{m,\rm BO}$, i.e., for (comparing Equations (6) and (11))

$$t > t_{\rm BO} = 0.05 \times 10^5 \frac{(M/M_\odot)^{0.6} R_{*,13}^{1.4}}{\kappa_{0.34}^{0.2} E_{51}^{0.9}} \ {\rm s}. \qquad (16)$$

This requirement also ensures that the ejecta shells have expanded and cooled significantly, and thus reached their terminal velocity v_f. For these times, the approximation of Equation (7) holds, and the radius of each shell is well approximated by $r = t\, v_f$.

The value of f_v deviates from 2 for large δ_m, due to the increasing curvature of the shells (e.g., Matzner & McKee 1999). Requiring the deviation not to exceed 30%, in which case the error in Equation (13) is smaller than 15%, implies limiting the analysis to times

$$t < (f_\rho/0.07)^{0.69}(M/M_\odot)\kappa_{0.34}^{0.5} E_{51}^{-0.5} \times t_{\rm fv}, \qquad (17)$$

where $t_{\rm fv} = 4.5 \times 10^6$ s and 1.2×10^5 s for $n = 3/2$ and $n = 3$ envelopes, respectively. Thus, the curvature effect is negligible on day–week timescale for $M \sim 10\, M_\odot$, and may be significant on day timescale only for low mass ejecta.

2.3. Photon Diffusion

Let us next examine the assumption that photon diffusion does not lead to strong deviations from adiabatic expansion below the photosphere. The size of a region around $r(\delta_m, t)$ over which the diffusion has a significant effect is $D(\delta_m, t) \simeq \sqrt{ct/3k\rho(\delta_m, t)}$. Thus, the radius $r_d = r(\delta_{m,d}, t)$ above which diffusion affects the flow significantly may be estimated as $D(\delta_m = \delta_{m,d}, t) = r(\delta_m = \delta_{m,d}, t)$. This gives

$$r_d(t) = 3.7 \times 10^{14} f_\rho^{-0.069} \frac{E_{51}^{0.45}\kappa_{0.34}^{0.1}}{(M/M_\odot)^{0.35}} t_5^{0.79} \ {\rm cm} \ \left(n = \frac{3}{2}\right),$$

$$r_d(t) = 3.8 \times 10^{14} f_\rho^{-0.04} \frac{E_{51}^{0.44}\kappa_{0.34}^{0.12}}{(M/M_\odot)^{0.32}} t_5^{0.75} \ {\rm cm} \ (n = 3). \qquad (18)$$

This radius is similar to, and somewhat larger than, the photospheric radius given by Equation (12). The rapid increase of the diffusion time, $\sim 3\kappa\rho r^2/c$, at smaller radii implies that diffusion does not significantly affect the fluid energy density below the photosphere. Next, we note that in regions where the diffusion time is short, the luminosity carried by radiation, $L \propto r^2 dp/d\tau$, is expected to be independent of radius. The steep dependence of the density on radius ($d\ln\rho/d\ln r \sim -10$) then implies that the energy density roughly follows $p \propto \tau$, i.e., $T \propto \tau^{1/4}$. This temperature profile is close to the adiabatic profiles derived in Section 2.1, for which $T \propto \tau^{0.28}$ and $\tau^{0.27}$ for $n = 3$ and $3/2$, respectively. Thus, diffusion does not lead to a significant modification of the pressure and temperature profiles also at radii where the diffusion time is short.

The validity of the above conclusions may be tested by using the self-similar solutions of Chevalier (1992), which describe the diffusion of photons in an expanding envelope with a density following $\rho \propto r^{-m}t^{m-3}$ and initial pressure $p \propto r^{-l}t^{l-4}$. The evolution of the ejecta density and pressure derived in Section 2.1 follows, for $v_f t \gg R_*$, $\rho = Br^{-m}t^{m-3}$ with $m-3 = (1+n)/n\beta_1$, and $p = Ar^{-l}t^{l-4}$ with $l = (3\gamma-2)+(\gamma+n)/n\beta_1$, where $\gamma = 4/3$. Applying the solutions of Chevalier (1992) to these profiles, one finds the same r_d as given by Equation (18)

and

$$L_c = 9.6 \times 10^{42} \frac{E_{51}^{0.91} R_{*,13}}{f_\rho^{0.17}(M/M_\odot)^{0.74}\kappa_{0.34}^{0.82}} t_5^{-0.35} \ {\rm erg\ s}^{-1}, \qquad (19)$$

for $n = 3$ and

$$L_c = 1.0 \times 10^{43} \frac{E_{51}^{0.96} R_{*,13}}{f_\rho^{0.28}(M/M_\odot)^{0.87}\kappa_{0.34}^{0.91}} t_5^{-0.17} \ {\rm erg\ s}^{-1}, \qquad (20)$$

for $n = 3/2$. (The parameter q of the self-similar solutions is $q = 0.495$ and 0.683 for $n = 3$ and $n = 3/2$, respectively. The density and pressure coefficients are $A = 2.95E^{3.89}R_*f^{-0.44}M^{-2.89}$, $53.7E^{4.95}R_*f^{-0.89}M^{-3.95}$ and $B = 100E^{3.59}f^{-0.33}M^{-2.59}$, $10^3 E^{4.37}f^{-0.67}M^{-3.37}$ for $n = 3$ and $n = 3/2$, respectively.)

The parameter dependence of L_c derived using the self-similar diffusion solutions is similar to that obtained by the simple model of Section 2.2, and the normalization of L_c derived using the self-similar diffusion solutions differs from the results of Section 2.2, Equations (15) and (14), by $\approx 10\%$. The effective temperatures derived from the diffusion solutions, via $L = 4\pi r_{\rm ph}^2\sigma T^4$, differ from those derived in the previous section by 1%–5%. Thus, the effects of diffusion on the luminosity and on the effective temperature are small, as expected. It is important to emphasize in this context that since the diffusion approximation breaks down near the photosphere, the results obtained using the self-similar diffusion solutions are not necessarily more accurate than those derived (e.g., in the previous section) by neglecting photon diffusion below the photosphere. Improving the accuracy of the simple model requires a transport, rather than a diffusion, description of the photon propagation. The differences between the results obtained neglecting diffusion and including it may be considered as a rough estimate of the inaccuracy of the model.

Finally, the following note is in place here. The results of Chevalier (1992) for L and r_d (Equations (3.19) and (3.20)) are different both in normalization and in scaling from those derived here. This is due to some typographical errors in earlier equations of that paper. When corrected, in Chevalier & Fransson (2008), the results obtained using the diffusion solutions are similar to those obtained in Waxman et al. (2007) and here. The difference in the numerical coefficient of the photospheric temperature, Equation (19) of Waxman et al. (2007) and Equation (5) of Chevalier & Fransson (2008), is mainly due to the typo in Equation (19) of Waxman et al. (2007), which is corrected in Equation (13) above.

3. MODEL EXTENSIONS

The approximation of space- and time-independent opacity is justified at early times, when the envelope is highly ionized and the opacity is dominated by Thomson scattering. On a day timescale, the temperature of the expanding envelope drops to ~ 1 eV, see Equation (13). At this temperature, significant recombination may take place, especially for He-dominated envelopes, leading to a significant modification of the opacity. The model presented in Section 2 is generalized in Section 3.1 to include a more realistic description of the opacity. The deviation of the emitted spectrum from a blackbody spectrum, due to photon diffusion, is discussed in Section 3.2. A brief discussion of the effect of line opacity enhancement due to velocity gradients is given in Section 3.3. Throughout this section, we use the density structure given by Equation (1) with

$n = 3$, as appropriate for radiative envelopes. As explained in the previous section, the results are not sensitive to the exact value of n.

3.1. Varying Opacity

In order to obtain a more accurate description of the early UV/O emission, we use the mean opacity provided in the OP project tables (Seaton 2005). We replace Equation (10) with

$$\tau(\delta_m, t) = \int_{r(\delta_m, t)}^{\infty} dr \rho \, \kappa[T(\delta_m, t), \rho(\delta_m, t)], \qquad (21)$$

where $\kappa(T, \rho)$ is the Rosseland mean of the opacity, and solve $\tau(\delta_m = \delta_{m,\mathrm{ph}}, t) = 1$ numerically for the location of the photosphere. In order to simplify the comparisons with the suggested analytical models, in the remainder of this section we shall take the ejecta properties in the limit of Equation (8).

3.1.1. H Envelopes

Consider first explosions in H-dominated envelopes. In Figure 1, we compare the temperature of the photosphere calculated using the OP tables with the results given by Equation (13) for $\kappa = 0.34 \, \mathrm{cm^2 \, g^{-1}}$, corresponding to fully ionized H. The difference in T_{ph} obtained by the two methods is smaller than 10% for $T_{\mathrm{ph}} > 1$ eV. At lower temperatures, the $\kappa = 0.34 \, \mathrm{cm^2 \, g^{-1}}$ approximation leads to an underestimate of T_{ph}, by $\approx 20\%$ at 0.7 eV. This is due to the reduction in opacity accompanying H recombination. The reduced opacity implies that the photosphere penetrates deeper into the expanding envelope, to a region of higher temperature. The photospheric radius is not significantly affected and is well described by Equation (12).

3.1.2. He Envelopes

Let us consider other explosions in He-dominated envelopes. In this case, the constant opacity approximation does not provide an accurate approximation for T_{ph}. We therefore replace Equations (12) and (13) with an approximation which takes into account the reduction of the opacity due to recombination. On the timescale of interest, hour $\lesssim t \lesssim$ day, the photospheric temperature is in the energy range of $3 \, \mathrm{eV} \gtrsim T \gtrsim 1 \, \mathrm{eV}$. In this temperature range (and for the characteristic densities of the photosphere), the opacity may be crudely approximated by a broken power law:

$$\kappa = 0.085 \, \mathrm{cm^2 g^{-1}} \begin{cases} (T/1.07 \, \mathrm{eV})^{0.88} & T > 1.07 \, \mathrm{eV}, \\ (T/1.07 \, \mathrm{eV})^{10} & T \leqslant 1.07 \, \mathrm{eV}. \end{cases} \qquad (22)$$

Using this opacity approximation, we find that Equation (13) for the photospheric temperature is modified to

$$T_{\mathrm{ph}}(t) = \begin{cases} 1.33 \, \mathrm{eV} \, f_\rho^{-0.02} R_{*,12}^{0.20} t_5^{-0.38} & T_{\mathrm{ph}} \geqslant 1.07 \, \mathrm{eV}, \\ 1.07 \, \mathrm{eV}(t/t_b)^{-0.12} & T_{\mathrm{ph}} < 1.07 \, \mathrm{eV}. \end{cases} \qquad (23)$$

Here, $R_* = 10^{12} R_{*,12}$ cm, and t_b is the time at which $T_{\mathrm{ph}} = 1.07$ eV, and we have neglected the dependence on E and M, which is very weak. The photospheric radius, which is less sensitive to the opacity modification, is approximately given by

$$r_{\mathrm{ph}}(t) = 2.8 \times 10^{14} f_\rho^{-0.038} E_{51}^{0.39} (M/M_\odot)^{-0.28} t_5^{0.75} \, \mathrm{cm}. \qquad (24)$$
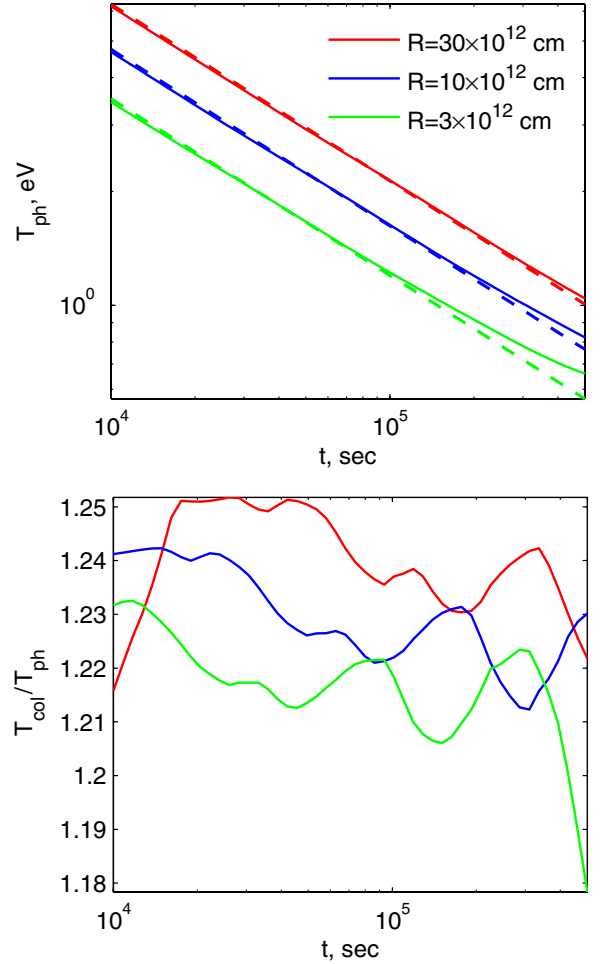

Figure 1. Photospheric temperature (top panel) and the ratio of color to effective (=photospheric) temperatures (bottom panel) for explosions in H-dominated envelopes (H with the solar composition of heavier elements). The top panel compares the analytic approximation of Equation (13) for fixed, $\kappa = 0.34 \, \mathrm{cm^2 \, g^{-1}}$, opacity (dashed lines) with the numerical solution of Equation (21) using OP table opacities (solid lines). The color to effective temperature ratio was calculated as explained in Section 3.2. Results are shown for $E = 10^{51}$ erg, $M = 1 \, M_\odot$, and three progenitor radii, $\{30, 10, 3\} \times 10^{12}$ cm.

(A color version of this figure is available in the online journal.)

Here, we have neglected the dependence on R_*, which is weak. For $T_{\mathrm{ph}} > 1.07$ eV, the bolometric luminosity is given by

$$L = 3.3 \times 10^{42} \frac{E_{51}^{0.84} R_{*,13}^{0.85}}{f_\rho^{0.15}(M/M_\odot)^{0.67}} t_5^{-0.03} \, \mathrm{erg \, s^{-1}}. \qquad (25)$$

The deviation of f_v from the assumed value of 2 for large δ_m (discussed in Section 2.2) has only a negligible effect on Equations (23) and (25).

In Figure 2, we compare the approximation of Equation (23) for T_{ph} with a numerical calculation using the OP opacity tables. The approximation of Equation (23) holds to better than 8% down to $T_{\mathrm{ph}} \simeq 1$ eV. The temperature does not decrease significantly below $\simeq 1$ eV due to the rapid decrease in opacity below this temperature, which is caused by the nearly complete recombination.

The following comment is in place here. The strong reduction in opacity due to He recombination implies that the photosphere reaches deeper into the envelope, to larger values of δ_m. The plus signs in Figure 2 denote the time at which $\delta_{m,\mathrm{ph}} = 0.1$. For such a large mass fraction, the initial density profile is no
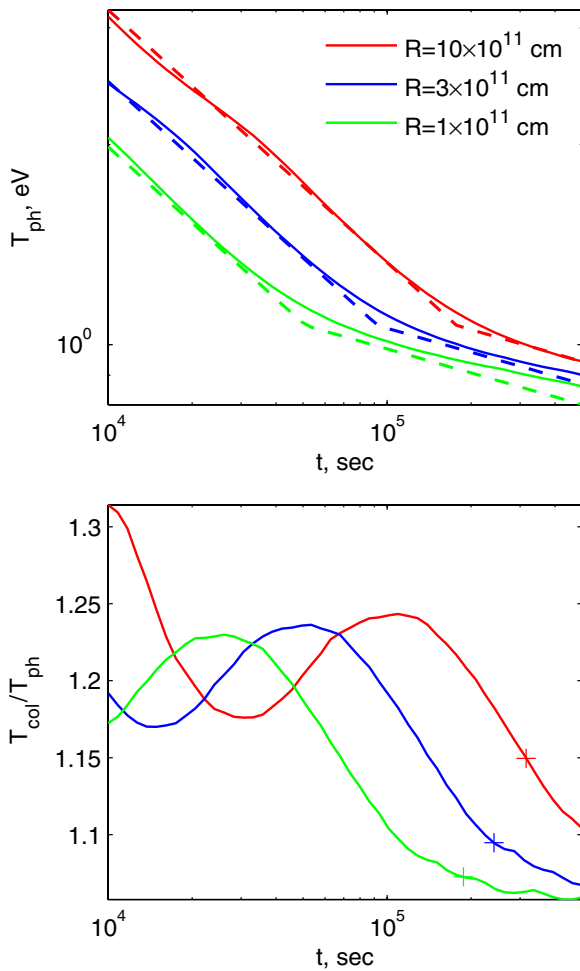
Figure 2. Photospheric temperature (top panel) and the ratio of color to effective (=photospheric) temperatures (bottom panel) for explosions in He-dominated envelopes (helium mass fraction of 98%, C/N/O/Ne fractions taken from Figure 18 of Meynet & Maeder 2003). The top panel compares the analytic approximation of Equation (23) (dashed lines) with the numerical solution of Equation (21) using OP table opacities (solid lines). The color to effective temperature ratio was calculated as explained in Section 3.2. Results are shown for $E = 10^{51}$ erg, $M = 1\,M_\odot$, and three progenitor radii, 10, 3, 1 $\times\,10^{11}$ cm. The + sign indicates the time at which $\delta m_{\rm ph} = 0.1$.

(A color version of this figure is available in the online journal.)

longer described by Equation (1) and the evolution of the ejecta is no longer given by equations of Section 2.1. This further complicates the model for the emission on these timescales (see Section 6.1 for further discussion).

3.1.3. He–C/O Envelopes

Let us consider next envelopes composed of a mixture of He and C/O. At the relevant temperature and density ranges, the C/O opacity is dominated by Thomson scattering of free electrons provided by these atoms, and is not very sensitive to the C:O ratio. Denoting by $1 - Z$ the He mass fraction, the C/O contribution to the opacity may be crudely approximated, within the relevant temperature and density ranges, by

$$\kappa = 0.043\,Z\ {\rm cm^2\,g^{-1}}(T/1\ {\rm eV})^{1.27}. \qquad (26)$$

This approximation holds for a 1:1 C:O ratio. However, since the opacity is not strongly dependent on this ratio, $T_{\rm ph}$ obtained using Equation (26) (Equation (27)) holds for a wide range of C:O ratios (see discussion at the end of this subsection). At the

regime where the opacity is dominated by C/O, Equation (13) is modified to

$$T_{\rm ph}(t) = 1.5\ {\rm eV}\,f_\rho^{-0.017}Z^{-0.2}R_{*,12}^{0.19}t_5^{-0.35}. \qquad (27)$$

In the absence of He, i.e., for $Z = 1$, $T_{\rm ph}$ is simply given by Equation (27). For a mixture of He–C/O, $Z < 1$, $T_{\rm ph}$ may be obtained as follows. At high temperatures, where He is still ionized, the He and C/O opacities are not very different and $T_{\rm ph}$ obtained for a He envelope, Equation (23), is similar to that obtained for a C/O envelope, Equation (27). At such temperatures, we may use Equation (23) for an envelope containing mostly He, and Equation (27) with $Z = 1$ for an envelope containing mostly C/O (a more accurate description of the Z-dependence may be straightforwardly obtained by an interpolation between the two equations). At lower temperatures, the He recombines and the opacity is dominated by C/O. At these temperatures, $T_{\rm ph}$ is given by Equation (27) with the appropriate value of Z. The transition temperature is given by

$$T_{\rm He-C/O} = 1\,Z^{0.1}\ {\rm eV}. \qquad (28)$$

The photospheric radius, which is less sensitive to the opacity variations, is well approximated by Equation (24). At the stage where the opacity is dominated by C/O, the bolometric luminosity is given by

$$L = 4.7 \times 10^{42}\,\frac{E_{51}^{0.83}R_{*,13}^{0.8}}{f_\rho^{0.14}Z^{0.63}(M/M_\odot)^{0.67}}t_5^{-0.07}\ {\rm erg\,s^{-1}}. \qquad (29)$$

The deviation of f_v from the assumed value of 2 for large δ_m (discussed in Section 2.2) does not significantly affect the results of Equations (27) and (28), but may significantly affect the result given in Equation (29). Equations (17), (26), and (27) indicate that for an explosion with $M = 10\,M_\odot$ and $E_{51} = 1$, the luminosity will be reduced by a factor of ~2 (compared to the predictions of Equation (29)) when $T_{\rm ph} \approx 1$ eV. This further complicates the model for the emission on these timescales. See Section 6.1 for further discussion.

In Figures 3 and 4, we compare the analytic approximation for $T_{\rm ph}$ derived above to the results of numerical calculations using the OP opacity tables. For the C/O envelopes (Figure 3), the approximation of Equation (27) holds to better than 6% down to $T_{\rm ph} \simeq 0.5$ eV. For the $Z = 0.3$ mixed He–C/O envelopes (Figure 4), the approximations obtained by using Equations (23) and (27) with a transition temperature given by Equation (28) hold to better than 10% down to $T_{\rm ph} \simeq 0.8$ eV. Using similar comparisons for different compositions, we find that similar accuracies are obtained over the range $0.7 > Z > 0.3$, and for increasing or decreasing the C:O ratio by an order of magnitude.

3.2. Color versus Effective Temperature

We have shown in Section 2.3 that photon diffusion is not expected to significantly affect the luminosity. Such diffusion may, however, modify the spectrum of the emitted radiation. We discuss below in some detail the expected modification of the spectrum.

For the purpose of this discussion, it is useful to define the "thermalization depth," $r_{\rm ther}$, and the "diffusion depth," $r_{\rm diff}$. $r_{\rm ther}(t) < r_{\rm ph}(t)$ is defined as the radius at which photons that reach $r_{\rm ph}(t)$ at t "thermalize," i.e., the radius from which photons may reach the photosphere without being absorbed on the way. This radius may be estimated as the radius for which $\tau_{\rm sct}\tau_{\rm abs} \approx 1$
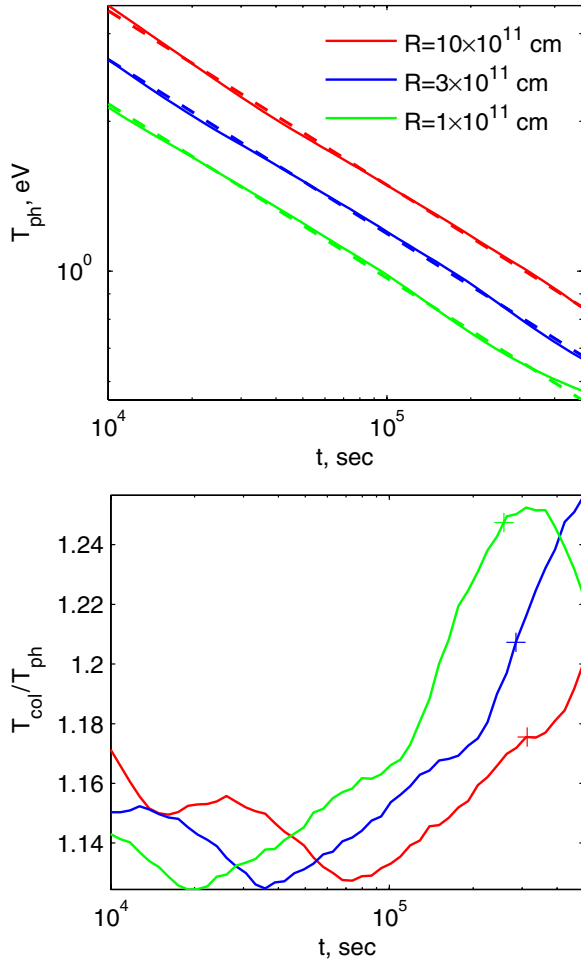
Figure 3. Photospheric temperature (top panel) and the ratio of color to effective (=photospheric) temperatures (bottom panel) for explosions in a C/O envelopes (1:1 C:O ratio). The top panel compares the analytic approximation of Equation (27) (dashed lines) with the numerical solution of Equation (21) using OP table opacities (solid lines). The color to effective temperature ratio was calculated as explained in Section 3.2. Results are shown for $E = 10^{51}$ erg, $M = 1 \, M_\odot$, and three progenitor radii, 10, 3, 1×10^{11} cm. The + sign indicates the time at which $\delta m_{\rm ph} = 0.1$.

(A color version of this figure is available in the online journal.)

(Mihalas & Mihalas 1984), where $\tau_{\rm sct}$ and $\tau_{\rm abs}$ are the optical depths for scattering and absorption provided by plasma lying at $r > r_{\rm ther}(t)$. $r_{\rm ther}$ is thus approximately given by

$$3(r_{\rm ther} - r_{\rm ph})^2 \kappa_{\rm sct}(r_{\rm ther}) \kappa_{\rm abs}(r_{\rm ther}) \rho^2(r_{\rm ther}) = 1, \qquad (30)$$

where $\kappa_{\rm sct}$ and $\kappa_{\rm abs}$ are the scattering and absorption opacities, respectively. (Typically, the opacity is dominated by electron scattering.) $r_{\rm diff}$ is defined as the radius (below the photosphere) from which photons may escape (i.e., reach the photosphere) over a dynamical time (i.e., over t, the timescale for significant expansion). We approximate $r_{\rm diff}$ by

$$r_{\rm ph} = r_{\rm diff} + \sqrt{c \, t / 3 \kappa_{\rm sct}(r_{\rm diff}) \rho(r_{\rm diff})}, \qquad (31)$$

where c is the speed of light.

For $r_{\rm diff} < r_{\rm ther}$, photons of the characteristic energy $3T(r_{\rm ther}, t) > 3T_{\rm ph}$ will reach the photosphere, while for $r_{\rm ther} < r_{\rm diff}$ photons of the characteristic energy $3T(r_{\rm diff}, t) > 3T_{\rm ph}$ will reach the photosphere. Thus, the spectrum will be modified from a blackbody at $T_{\rm ph}$ and its color temperature will be $T_{\rm col} > T_{\rm ph}$.
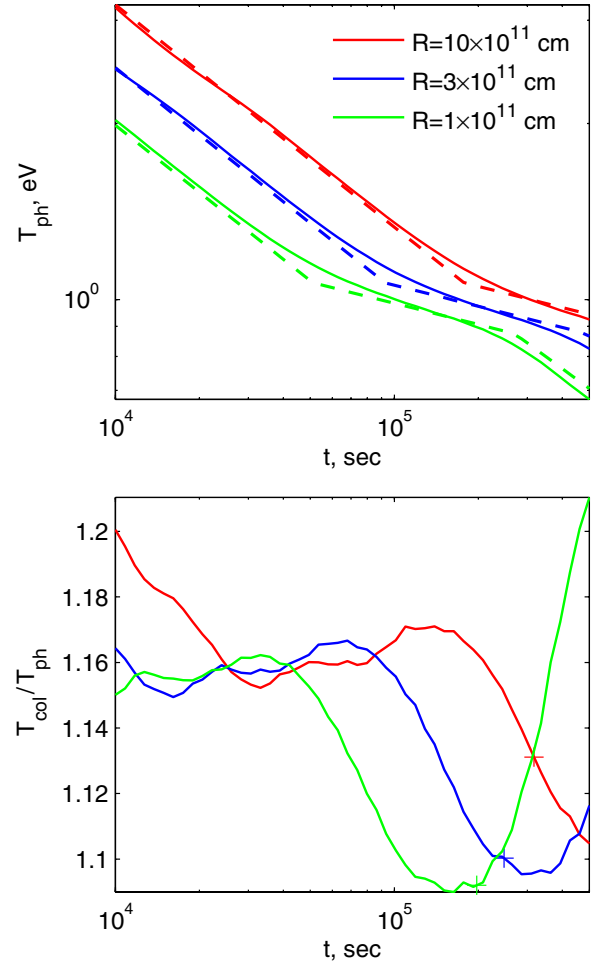
Figure 4. Photospheric temperature (top panel) and the ratio of color to effective (=photospheric) temperatures (bottom panel) for explosions in a He–C/O envelopes ($1 - Z = 0.7$ He mass fraction, 2:1 C:O ratio). The top panel compares the analytic approximations obtained using Equations (23) and (27) with a transition temperature given by Equation (28) (dashed lines) with the numerical solutions of Equation (21) using OP table opacities (solid lines). The color to effective temperature ratio was calculated as explained in Section 3.2. Results are shown for $E = 10^{51}$ erg, $M = 1 \, M_\odot$, and three progenitor radii, 10, 3, 1×10^{11} cm. The + sign indicates the time at which $\delta m_{\rm ph} = 0.1$.

(A color version of this figure is available in the online journal.)

We approximate in what follows $T_{\rm col} = T(r_{\rm ther})$ for $r_{\rm diff} < r_{\rm ther}$ and $T_{\rm col} = T(r_{\rm diff})$ for $r_{\rm diff} > r_{\rm ther}$.

The lower panels of Figures 1–4 present the ratio $T_{\rm col}/T_{\rm ph}$ for the various envelope compositions considered. For this calculation, we have assumed that the scattering opacity is dominated by Thomson scattering of free electrons, used the electron density (as the function of density and temperature) provided by the OP tables for determining $\kappa_{\rm sct}$, and estimated $\kappa_{\rm abs} = \kappa - \kappa_{\rm sct}$. (Recall that κ is the Rosseland mean of the opacity.) It would have been more accurate to use an average of the absorptive opacities over the relevant wave bands, which are not provided by the OP table. However, since the dependence of the color temperature on the absorptive opacity is weak, $T_{\rm col} \propto \kappa_{\rm abs}^{(-1/8)}$, the corrections are not expected to be large. The figures imply that over the relevant timescale, $t \lesssim 1$ day,

$$f_T \equiv T_{\rm col}/T_{\rm ph} \approx 1.2. \qquad (32)$$

Using Equation (32) with Equations (13), (23), and (27) for the photospheric (effective) temperature, the progenitor radius

may be approximately inferred from the color temperature by

$$R_* \approx 0.70 \times 10^{12} \left[\frac{T_{\rm col}}{(f_T/1.2)\,{\rm eV}}\right]^4 t_5^{1.9} f_\rho^{0.1}\ {\rm cm} \qquad (33)$$

for H envelopes,

$$R_* \approx 1.2 \times 10^{11} \left[\frac{T_{\rm col}}{(f_T/1.2)\,{\rm eV}}\right]^{4.9} t_5^{1.9} f_\rho^{0.1}\ {\rm cm} \qquad (34)$$

for He envelopes with $T > 1.07$ eV, and

$$R_* \approx 0.58 \times 10^{11} \left[\frac{T_{\rm col}}{(f_T/1.2)\,{\rm eV}}\right]^{5.3} t_5^{1.9} f_\rho^{0.1} Z\ {\rm cm} \qquad (35)$$

for He–C/O envelopes when the C/O opacity dominates. (The transition temperature is given in Equation (28).)

3.3. Expansion Opacity

We have neglected in our analysis the effective broadening of atomic lines due to the velocity gradients in the outflow. Line broadening may have a significant effect on the opacity and on the observed emission (Karp et al. 1977; Wagoner et al. 1991; Eastman & Pinto 1993), as well as on the dynamics (e.g., in the case of stellar winds, see Friend & Castor 1983). We give below a crude estimate of the line-broadening effects for the problem of interest here. A detailed analysis of line broadening, which requires detailed numerical calculations (see, e.g., Section 6.9 of Castor 2004), is beyond the scope of this manuscript.

The analysis of Wagoner et al. (1991) shows that the effective line opacity introduced by the velocity gradients may significantly affect the Rosseland mean opacity (at the relevant densities and velocity gradients, see their Figures 5 and 6) at temperatures where recombination leads to a large reduction of the Thomson electron scattering opacity. The main contribution to this "expansion opacity" is from resonant line scattering of Fe group elements. As explained in Section 3.1, the main effect that recombination introduces to our analysis is the penetration of the photosphere to shells of high enough temperatures where significant ionization is maintained. Since the opacity enhancement due to velocity gradient effects does not prevent the strong reduction of the opacity due to recombination, it will not prevent the penetration of the photosphere to a region of significant ionization. Nevertheless, the enhanced line opacity may introduce an order unity increase of the opacity at temperatures close to the recombination temperature at short, $\lambda < 0.25\,\mu$, wavelengths (see Figures 6 and 7 of Wagoner et al. 1991). A detailed analysis of this effect is beyond the scope of this manuscript.

We should note, nevertheless, that the effective line opacity enhancement due to velocity gradients may be smaller in our case compared to the estimates of earlier analyses. To show this, let us examine the following heuristic derivation of the effective broadening of atomic lines. Consider a photon that travels outward/inward in the region of relatively low optical depth. Due to the velocity gradient of the expanding ejecta, the photon frequency as measured in the plasma rest frame is shifted as it propagates by $dv/v = -dv/c = -(\partial v/\partial r)dr/c = -(\partial v/\partial r)dt$, where $dv = (\partial v/\partial r)dr$ is the velocity difference across dr, and we neglect the plasma speed with respect to that of the photon in setting $dr = cdt$. Assuming that a photon is absorbed/scattered as its frequency is shifted across that of a line, then the probability for scattering/absorption is $dP = dv(dN/dv)$, where dN/dv is the line "density" per

unit frequency. The resulting photon mean free path is therefore $l^{-1} \sim dP/cdt \sim c^{-1}|\partial v/\partial r|v(dN/dv)$. For $v = r/t$, which is valid at late time, we have

$$l_\nu^{-1} \sim \frac{|\partial v/\partial r|}{c} \nu(dN/d\nu) = (ct)^{-1}\nu(dN/d\nu) \qquad (36)$$

(compare, e.g., to Equation (3.10) of Wagoner et al. 1991). The photon is absorbed/scattered provided the line optical depth is large enough. Neglecting the natural width of the lines, we may replace the line opacity with $\kappa_\nu = \kappa_l \nu_0 \delta(\nu - \nu_0)$. Denoting $\nu' = (1 - dv/c)\nu$, we obtain

$$\tau_l \sim \int cdt'\rho\kappa_{\nu'} \approx \int \frac{d\nu'}{\nu}\frac{c}{\partial v/\partial r}\rho\kappa_{\nu'}$$
$$\approx \frac{c}{\partial v/\partial r}\rho\kappa_l = ct\rho\kappa_l. \qquad (37)$$

Thus, the line should be "counted" in determining $dN/d\nu$, if $ct\rho\kappa_l \gg 1$ (compare, e.g., to Equations (3.10) and (2.7) of Wagoner et al. (1991), and Equation (9) of Friend & Castor 1983).

The analyses of Wagoner et al. (1991) and of Karp et al. (1977) are "local." That is, it is assumed there that as the photon's frequency is shifted by an amount comparable to the strong line separation, the parameters of the plasma within which it propagates do not change (the Karp et al. 1977, assumptions are in fact more restrictive). We have made the same assumption in deriving the final result of Equation (37). However, the validity of this assumption is not obvious in our case. For the self-similar ejecta profiles described in Section 2.1, ρ and T are steeply falling functions of v_f, ρ is roughly proportional to v_f^{-10} and T is roughly proportional to v_f^{-3}. Thus, as the photon moves outward and its frequency is shifted (in the plasma frame) by $\sim v/c$ (i.e., by $dr/r \sim 1$), ρ and T drop by factors of 10^3 and 10^1, respectively. This implies that τ_l may be significantly smaller than given by Equation (36).

4. REMOVING THE EFFECTS OF REDDENING

We show in this section that the effects of reddening on the observed UV/O signal may be removed using the UV/O light curves. This is particularly important for inferring R_*, since $R_* \propto T_{\rm col}^\alpha$ with $4 \lesssim \alpha \lesssim 5$ (see Equations (13), (23), and (27)).

The model specific intensity, f_λ, is given by

$$f_\lambda(\lambda, t) = \left(\frac{r_{\rm ph}}{D}\right)^2 \sigma T_{\rm ph}^4 \frac{T_{\rm col}}{hc} g_{BB}(hc/\lambda T_{\rm col})e^{-\tau_\lambda}, \qquad (38)$$

where

$$g_{BB}(x) = \frac{15}{\pi^4}\frac{x^5}{e^x - 1}, \qquad (39)$$

D is the distance to the source, and τ_λ is the extinction optical depth at λ. Let us define $t_\lambda(t, \lambda)$ by

$$\lambda T_{\rm col}[t = t_\lambda(t, \lambda)] = \lambda_0 T_{\rm col}(t), \qquad (40)$$

for some chosen λ_0. With this definition, the scaled light curves,

$$\tilde{f}_\lambda[\lambda, t_\lambda(t, \lambda)] \equiv \left[\frac{D}{r_{\rm ph}(t_\lambda)}\right]^2 \left[\frac{T_{\rm col}(t_\lambda)}{T_{\rm ph}(t_\lambda)}\right]^4 \left[\frac{T_0}{T_{\rm col}(t_\lambda)}\right]^5$$
$$\times f_\lambda(\lambda, t_\lambda) \qquad (41)$$

(where T_0 is an arbitrary constant) are predicted to be the same for any λ up to a factor $e^{-\tau_\lambda}$,

$$\tilde{f}_\lambda[\lambda, t_\lambda(t, \lambda)] = \sigma T_0^4 \frac{T_0}{hc} g_{BB}[hc/\lambda_0 T_{col}(t)] \times e^{-\tau_\lambda}. \quad (42)$$

Let us consider now how the scalings defined above allow one to determine the relative extinction in cases where the model parameters $\{E, M, R_*\}$ are unknown, and hence $\{T_{col}, T_{ph}, r_{ph}\}(t)$, which define the scalings, are also unknown. For simplicity, let us first consider the case where the time dependence of the photospheric radius and temperature are well approximated by power laws:

$$r_{ph} \propto t^{\alpha_r}, \quad T_{ph} \propto t^{-\alpha_T}, \quad (43)$$

and the ratio T_{col}/T_{ph} is independent of time. This is a good approximation for the time dependence of r_{ph} in general, and for the time dependence of T_{col} and T_{ph} for $T_{ph} > 1$ eV (see Equations (12), (13), (23), (24), (27), and (32)). In this case, Equation (40) gives

$$t_\lambda(t, \lambda) = \left(\frac{\lambda}{\lambda_0}\right)^{1/\alpha_T} t, \quad (44)$$

and Equation (41) may be written as

$$\tilde{f}_\lambda[\lambda, t_\lambda(t, \lambda)] = \text{const.} \times \left(\frac{\lambda}{\lambda_0}\right)^{(-2\alpha_r + 5\alpha_T)/\alpha_T} t^{-2\alpha_r + 5\alpha_T}$$
$$\times f_\lambda\left[\lambda, \left(\frac{\lambda}{\lambda_0}\right)^{1/\alpha_T} t\right]. \quad (45)$$

The value of the constant that appears in Equation (45), for which the normalization of $\tilde{f}_\lambda$ is that given by Equation (42), is not known, since it depends on the model parameters $\{E, M, R_*\}$. However, for any choice of the value of the constant, $\tilde{f}_\lambda$ defined by Equation (45) is predicted by the model to be given by Equation (42) up to a wavelength-independent multiplicative factor. Thus, the ratio of the scaled fluxes defined in Equation (45) determines the relative extinction:

$$\frac{\tilde{f}_\lambda[\lambda_1, t_\lambda(t, \lambda_1)]}{\tilde{f}_\lambda[\lambda_2, t_\lambda(t, \lambda_2)]} = e^{\tau_{\lambda_2} - \tau_{\lambda_1}}. \quad (46)$$

Let us consider next the case where the time dependence of T_{col} and T_{ph} is not a simple power law. We have shown in Sections 2 and 3 that T_{col} and T_{ph} are determined by the composition and progenitor radius R_*, and are nearly independent of E and M. Adopting some value of R_*, Equation (40) may be solved for $t_\lambda(t, \lambda; R_*)$, and Equation (41) may be written as

$$\tilde{f}_\lambda[\lambda, t_\lambda(t, \lambda; R_*)] = \text{const.} \times t^{-2\alpha_r} T_{ph}(t_\lambda)^{-4} T_{col}(t_\lambda)^{-1}$$
$$\times f_\lambda(\lambda, t_\lambda). \quad (47)$$

The model predicts therefore that scaling the observed flux densities using the correct value of R_*, the observed light curves at all wavelengths should be given by Equation (42), up to a multiplicative wavelength-independent constant. For this value of R_*, the ratio of the scaled fluxes at different wavelengths is independent of t and given by Equation (46). The value of R_* may therefore be determined by requiring the ratios of scaled fluxes to be time independent, and the relative extinction may then be inferred from Equation (46). We use this method in Section 6 for determining R_* and the extinction curve for SN 2008D.
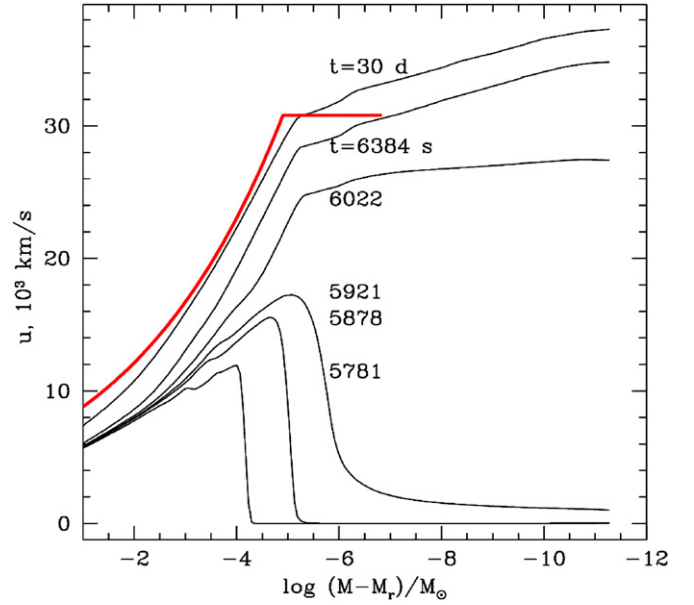

Figure 5. Ejecta velocity profiles at different times, pre- and post-shock breakout, obtained in the 14E1.3 model calculation of Blinnikov et al. (2000), compared with the Matzner & McKee (1999) approximation (red line) for the post-breakout velocity profile used in our analytical model, given by Equation (3) for $\delta_m > \delta_{m,BO}$ and assumed uniform at smaller δ_m (see Equation (6)).

(A color version of this figure is available in the online journal.)

5. COMPARISON TO OBSERVATIONS AND SIMULATIONS: RSG AND BSG PROGENITORS

5.1. SN1987A–A BSG Progenitor

Following the observations of SN 1987A, many numerical calculations modeling its light curve have been carried out (see, e.g., Hauschildt & Ensman 1994). The latest and most comprehensive of these calculations was carried out by Blinnikov et al. (2000), and it provides UBV light curves from the time of breakout to several months following the explosion. The Blinnikov et al. (2000) radiation-hydrodynamics calculation, which includes a detailed treatment of the opacities and a multi-group transport approximation for the propagation of radiation, should, to our understanding, capture all the relevant physics.

In Figures 5 and 6, we compare the results of our simple model to those of the detailed numerical calculations of Blinnikov et al. (2000). We use the same progenitor parameters as those used in Blinnikov et al. (2000): a BSG (H envelope with $n = 3$, $f_\rho = 1$) of radius $R_* = 3.37 \times 10^{12}$ cm, ejecta mass $M = 14.67\, M_\odot$, and explosion energies $E = 1.03$ and 1.34×10^{51} erg for models 14E1 and 14E1.3, respectively (and composition as in the outer part of the progenitor given in Figure 2 of Blinnikov et al. 2000). Figure 5 compares the numerical velocity profile with the Matzner & McKee (1999) approximation we use in our model, given by Equation (3). The two agree to better than 10% over the relevant envelope mass fraction. In Figure 6, we compare the numerical early UBV light curves of Blinnikov et al. (2000) with the ones calculated in our model, using Equation (21) with the OP opacity (Seaton 2005). As can be seen in the figure, our analytic model gives fluxes which are larger by a factor of $\sim$2 than those of the numerical calculation. This difference may be due to differences between the OP opacities and those used by Blinnikov et al. (2000). The opacity given in Blinnikov et al. (1998) for $\rho = 10^{-13}$ g cm^{-3}, $T = 15{,}000°$ K, and solar metallicity is larger than the OP opacity
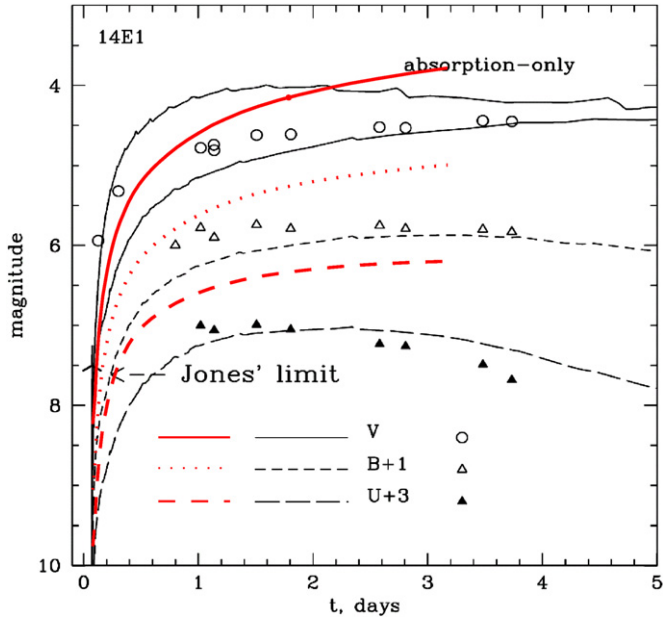
Figure 6. Comparison of early UBV measurements of SN 1987A with the 14E1 model calculations of Blinnikov et al. (2000) and with our model calculations (red line) for similar model parameters ($E_{B-V} = 0.15$ and a distance modulus of 18.5 assumed). The uppermost black curve in the figure (adapted from Blinnikov et al. 2000) is the V flux obtained in their 14E1A model calculation.

(A color version of this figure is available in the online journal.)

by roughly a factor of two. If a similar difference exists for the modified metallicity used in the SN1987A calculations, it would explain the luminosity discrepancy since the luminosity is roughly inversely proportional to κ, see Equation (15).

5.2. SNLS−04D2dc—An RSG Progenitor

The *GALEX* far-UV and near-UV measurements of the type IIp SNLS−04D2dc are shown in Figure 7. Given the relatively low signal-to-noise ratio, we do not attempt here to constrain the progenitor parameters using a detailed analysis of the UV emission (as we do for SN 2008D in Section 6). Rather, we show that the observed UV flux is consistent with that expected from an expanding shock heated envelope of an RSG progenitor, and compare our simple model predictions to those obtained using detailed numerical calculations. For the latter purpose, we use the numerical calculations described in Gezari et al. (2008).

Gezari et al. (2008) performed detailed numerical calculations, aimed at reproducing the early UV/O emission from the SNLS−04D2dc, the progenitor of which is most likely an RSG. Their calculation was performed in two stages. At the first stage, a hydrodynamic calculation of the explosion was performed using the one-temperature Lagrangian radiation-hydrodynamics code KEPLER (Weaver et al. 1978). At the second stage, the emission of radiation at time t was calculated by solving, using the multi-group radiation transport code CMFGEN (Dessart & Hillier 2005), the steady state radiation field for the hydrodynamic profiles obtained at time t, keeping the temperature profile fixed for $\tau > 20$ and allowing it to self-consistently change at smaller optical depths.

In Figure 8, we compare the Gezari et al. (2008) calculations with the results obtained by our model, using Equation (21) with the OP opacity (Seaton 2005). The progenitor parameters we use are: an RSG (H envelope with $n = 3/2$ and $f_\rho = 25$) of radius $R_* = 865\,R_\odot$, explosion energy $E_{51} = 1.44$, and the ejecta mass of $M = 8.9\,M_\odot$. The stellar radius is similar to that
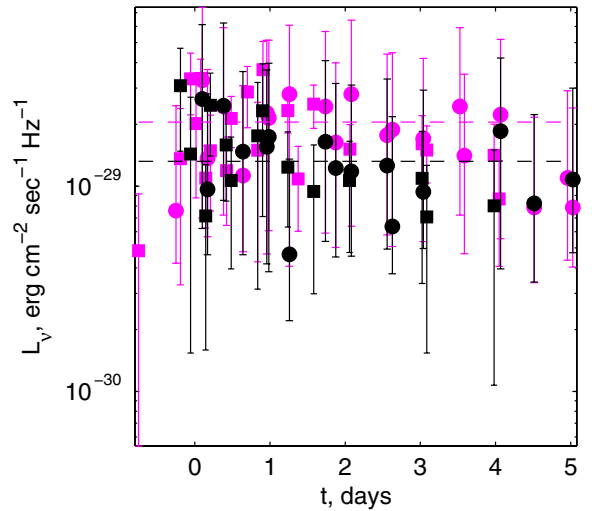

Figure 7. *GALEX* far-UV ($\lambda_{\rm eff} = 1539$ Å black) and near-UV ($\lambda_{\rm eff} = 2316$ Å magenta) observations of SNLS−04D2dc, not corrected for host and Galactic extinction. The photometric analyses of Gezari et al. (2008) and Schawinski et al. (2008) are shown in circles and squares, respectively. The dashed (black, magenta) lines show the (far-UV, near-UV) background levels inferred by Schawinski et al. (2008).

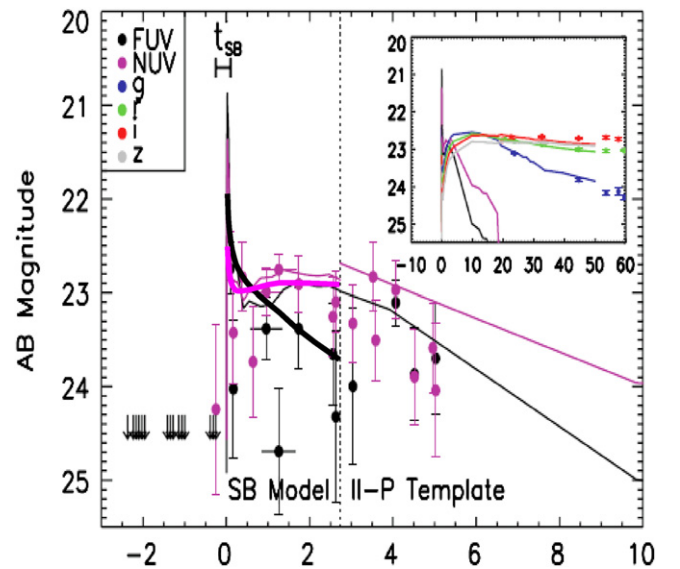(A color version of this figure is available in the online journal.)

Figure 8. Comparison of the numerical model calculations of Gezari et al. (2008) (thin lines) with our model calculations (over laid thick lines) for similar progenitor parameters and extinction (see the text for details). Due to the computationally demanding nature of the numerical calculation, the numerical model of Gezari et al. (2008) extends up to the time marked by the vertical dotted line (the thin curves at later times are a scaled SN II-P template).

(A color version of this figure is available in the online journal.)

used by Gezari et al. (2008), and $f_\rho = 25$ was chosen (based on a private communication with S. Gezari and L. Dessart, 2008) to provide an approximate description of the outer RSG envelope profile used in their calculation. The explosion energy and ejecta mass used in our model are 20% larger and smaller, respectively, than those used by Gezari et al. (2008), i.e., the E/M ratio is 40% larger in our calculation. This value was chosen to reproduce the observed luminosity. The light curves calculated by Gezari et al. (2008) were shifted by ~ -1.5 mag, i.e., the calculated luminosity was increased by a factor of ~ 4, to fit the observations. Since the luminosity is approximately proportional to E/M (see Equation (14)), this implies that for

a given E/M ratio our calculation predicts a luminosity that is larger than that of Gezari et al. (2008) by a factor of $\sim$3 (we have verified this by comparing the results of Gezari et al. 2008 to our model results for the same E/M ratio).

The following point should be noted here. Due to the large radius of the progenitor, the photosphere lies within the "breakout shell," i.e., $\delta_{m,\mathrm{ph.}} < \delta_{m,\mathrm{BO}}$ (see Equation (6)), up to $t = t_{\mathrm{BO}} \simeq 1.5$ d (see Equation (16)). Our simple model is not valid at $t < t_{\mathrm{BO}}$. However, we expect it to provide a reasonable approximation for the photospheric temperature and radius also at $t < t_{\mathrm{BO}}$, for the following reason. As long as the photosphere lies at $\delta_{m,\mathrm{ph.}} < \delta_{m,\mathrm{BO}}$, the diffusion time at the photosphere is short compared to t. In this case, we expect the spatial dependence of the radiation pressure to approximately follow $p \propto \tau$ (see Section 2.3), in which case the photospheric temperature is given by $aT_{\mathrm{ph}}^4 = 3p(\tau)/\tau$. Since, as explained in Section 2.3, the adiabatic pressure profile, $p \propto \tau^{1.1}$, is similar to that obtained for short diffusion time, $p \propto \tau$, and since the adiabatic pressure profile is valid at all times for $\delta_m \gg \delta_{m,\mathrm{BO}}$, we expect Equation (13) to provide a good approximation for T_{ph} also at $t < t_{\mathrm{BO}}$. The temporal dependence of r_{ph} is expected to be somewhat stronger, at $t < t_{\mathrm{BO}}$, than $r_{\mathrm{ph}} \propto t^{0.8}$ predicted by the simple adiabatic model, since the velocity profile at $\delta_{m,\mathrm{ph.}} < \delta_{m,\mathrm{BO}}$ is shallower than predicted by Equation (3). The largest deviation from the $r_{\mathrm{ph}} \propto t^{0.8}$ behavior would be obtained assuming uniform velocity at $\delta_{m,\mathrm{ph.}} < \delta_{m,\mathrm{BO}}$, which would yield $r_{\mathrm{ph}} \propto t$.

The factor of $\sim$2 discrepancy between the luminosity predicted by our model and that obtained by Gezari et al. (2008) is due to the fact that our model predicts a somewhat, $\sim$40%, larger velocity for the fast outer shells, and hence a larger photospheric radius. In a subsequent publication (I. Rabinak et al. 2011, in preparation), we examine the accuracy of the approximate ejecta density and velocity profiles described in Section 2.1 for a wide range of progenitor models.

6. THE EARLY UV/O EMISSION OF SN 2008D

The analysis of the early UV/O emission of SN 2008D is complicated by two major factors. First, the extinction is large. It was loosely constrained by Soderberg et al. (2008) to $0.4 < E(B - V) < 0.8$. This large extinction makes it difficult to extract the color temperature from the observations, and increases the uncertainty of the interpretation. The second complication arises from the fact that there is only one set of measurements in the UV at $t \lesssim 2$ days, and most of the relevant data points are at $t > 1$ d. This implies, as explained in Section 3.1, that the simple approximate solutions given by Equations (24) and (27) for the photospheric radius and temperature are not accurate. For both He and mixed He–C/O compositions the reduction in opacity due to He recombination at $\gtrsim 1$ d implies that the photosphere penetrates into the envelope beyond the range of validity of the approximation of Equation (1) for the initial density profile. For the analysis of SN 2008D, we will use therefore a more detailed description of the density and pressure profiles of the ejecta. We first describe the modified ejecta profiles we use in Section 6.1, and then analyze the SN 2008D observations using our model in Section 6.2. As we show there, the deviation of the ejecta profiles from the $\delta_m \to 0$ self-similar profiles described in Section 2.1 lead to modifications of the model predictions at $t \gtrsim 2$ d. Comparison of our results to some earlier work appears in Section 6.3.

6.1. Modified Ejecta Profiles

The derivations of r_{ph} and T_{ph} in Sections 2.2 and 3 are based on the self-similar model of Section 2.1 for the density and pressure profiles of the ejecta. This model, in which $p(v_f)$ and $\rho(v_f)$ are both roughly proportional to v_f^{-10}, is valid in the limit $\delta_m \to 0$ ($v_f \to \infty$). In order to extend the model to larger values of δ_m, we adopt the "harmonic-mean" model suggested by Matzner & McKee (1999). In this model, the density and pressure profiles are obtained by interpolating between the small δ_m (large v_f) self-similar power-law dependence of $p(v_f)$ and $\rho(v_f)$, and the power-law dependence $p(v_f) \propto v_f^{\alpha}$, $\rho(v_f) \propto v_f^{\beta}$ with $\alpha \approx 2$ and $\beta \approx -1$, obtained in the approximate analysis of Chevalier & Soker (1989) for the lower velocity ejecta. This power-law dependence is obtained by assuming that the shock propagating within the ejecta may be approximately described, for large δ_m, by the Primakoff self-similar solution (a particular, analytic, case of the Sedov–von Neumann–Taylor solutions for shock propagation into $\rho \propto r^{-\omega}$ density profiles, obtained for $\omega = 17/7$, e.g., Gaffet 1984; Bernstein & Book 1980), and by an approximate (self-similar) description of the post-breakout acceleration of the shocked plasma. The two power-law solutions describing the large and small v_f behavior of the density are matched in the Matzner & McKee (1999) "harmonic-mean" model at $\rho = \rho_{\mathrm{break}}$ and $v_f = v_{\rho\mathrm{break}}$, and the pressure profiles at $p = p_{\mathrm{break}}$ and $v_f = v_{p\mathrm{break}}$ (see Equations (46) and (47) of Matzner & McKee 1999). ρ_{break} and $v_{\rho\mathrm{break}}$ are determined by requiring the ejecta mass and (kinetic) energy to be equal to M and E, respectively. p_{break} and $v_{p\mathrm{break}}$ are determined in Matzner & McKee (1999) by examining numerical simulation results. We find that their parameter choice of p_{break} and $v_{p\mathrm{break}}$ leads to an overestimate of the temperature, compared to that of the self-similar $\delta_m \to 0$ solution, by $\sim$15% at $\delta_m = 10^{-3}$. We therefore modify the value of p_{break} to obtain the correct self-similar behavior at $\delta_m \to 0$.

The "harmonic-mean" density and temperature profiles obtained as described in the preceding paragraph are compared in Figure 9 with those of the $\delta_m \to 0$ self-similar solution. A significant deviation from the self-similar profiles is obtained for $\delta_m \gtrsim 0.1$. As discussed in Section 6.2, this deviation affects the model predictions for $t \gtrsim 2$ d. The accuracy of the "harmonic-mean" model was examined in Matzner & McKee (1999) by comparing it to the results of numerical calculations of the explosions of various RSG and BSG progenitors. Since it was found that this analytic model provides a good approximation for the envelope's profiles for different initial density structures of the progenitors, we expect the harmonic-mean model to provide a good approximation also for the SN 2008D envelope profiles. However, additional work, which is beyond the scope of this paper, is required in order to obtain a quantitative estimate of the accuracy of the approximation for $\delta_m > 0.1$.

6.2. Models versus Observations

Spectroscopic observations have constrained the fraction of hydrogen in the ejecta to $\lesssim 5 \times 10^{-4}\ M_\odot$ (Tanaka et al. 2009). We therefore consider below He and He–C/O envelopes. As explained in Section 4, the relative extinction may be inferred from the light curves at different frequencies. However, for the clarity of the presentation, we first analyze the data using two relative extinction curves that differ significantly in their short wavelength behavior, a Milky Way extinction curve with $R_v = 3.1$ (hereafter MW) and a Small Magellanic Cloud extinction curve (hereafter SMC; Cardelli et al. 1989), and only
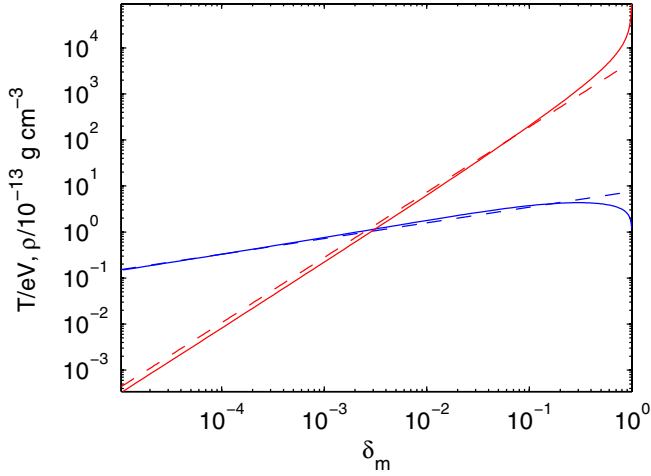
Figure 9. Comparison of the temperature and density profiles (in blue and red respectively) of the ejecta given by the self-similar solution of Section 2 (dashed lines) with those obtained in the "harmonic-mean" model described in Section 6.1 (solid lines), for an explosion of an $n = 3$ envelope with $E_{51} = 6$, $M = 7\,M_\odot$, and $R_* = 10^{11}$ cm, at $t = 10^5$ s.

(A color version of this figure is available in the online journal.)

later show how the extinction curve may be directly inferred from the data.

Figure 10 presents a comparison of the color temperature T_{col} and bolometric luminosity L inferred from the data with those obtained in our model for different progenitor and explosion parameters. We use the observations of *Swift*/UVTO (V, B, U, $UVW1$, $UVM2$, $UVW2$), Palomar (g, r, i, z) (both taken from Soderberg et al. 2008), and FLWO (B, V, r, i) (Modjaz et al. 2009). Since observations by different telescopes were carried out at different times, we interpolate the observations in different bands to times close to the observation times of the *Swift*/UVTO and the Palomar telescopes. In order to derive $T_{col}(t)$ and $L(t)$ from the observations, the measured fluxes should be corrected for extinction. We carry out this correction by (1) assuming a specific extinction curve (MW or SMC) and (2) determining the absolute value of the extinction by requiring T_{col} inferred from the observations to agree with the model prediction at $t \sim 2$ days. This implies that for each set of model parameters (E, M, R_*, envelope composition), a different value of the absolute extinction, $E(B - V)$ is chosen.

For all the models shown in the figure, we have used $E_{51} = 6$ and $M/M_\odot = 7$, as suggested by Mazzali et al. (2008) from
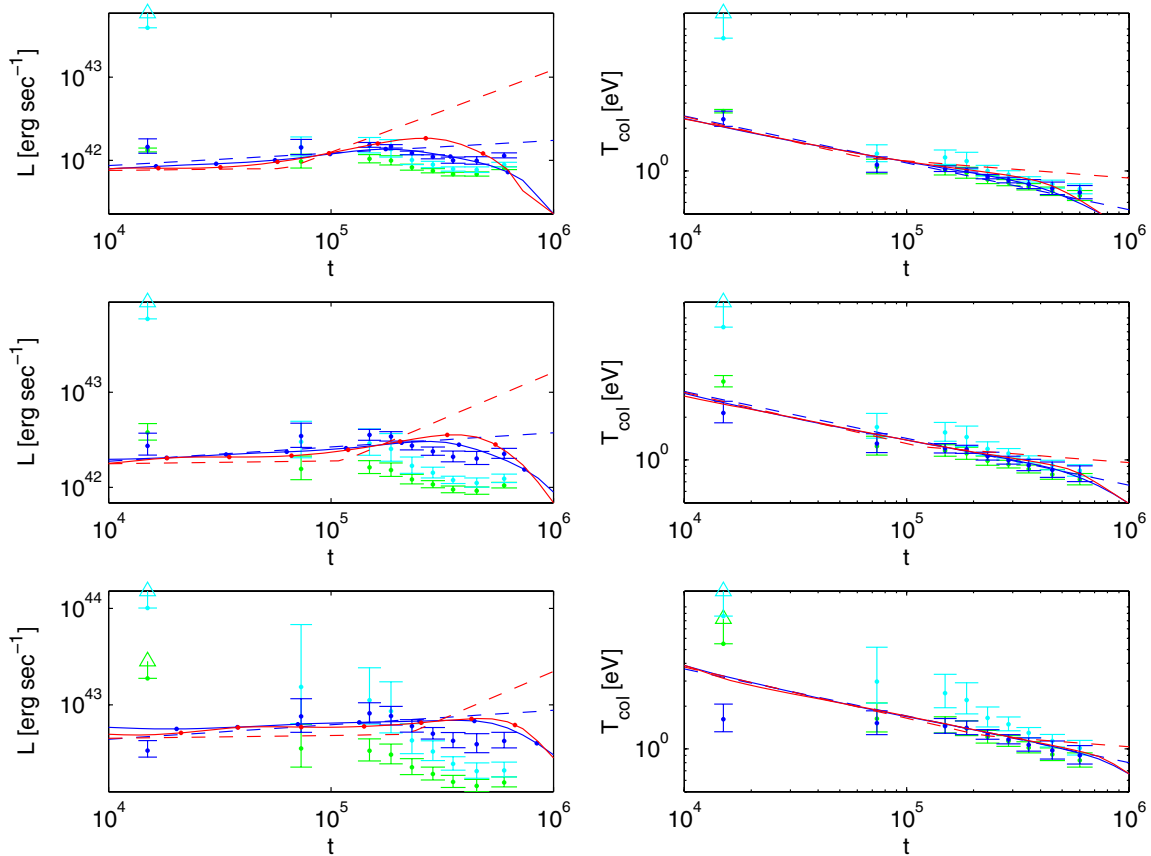

Figure 10. Comparison of the color temperature T_{col} and bolometric luminosity L inferred from the data with those obtained in our model for different progenitor and explosion parameters. Model results are shown for three progenitor radii, $R_* = 1, 3, 10 \times 10^{11}$ cm in the top, middle, and bottom panels, respectively, and for two envelope compositions, He-dominated (red) and mixed He–C/O composition with a He mass fraction $1 - Z = 0.3$ (blue). $E_{51} = 6$ and $M/M_\odot = 7$ (and $D = 27$ Mpc) are assumed for all models. Both the simple analytic approximations for L and T_{col} given in Section 3.1 are shown, which are based on the self-similar ejecta profiles of Section 2.1 (dashed lines), and L and T_{col} obtained solving Equations (21), (30), and (31) with the OP opacity tables for the modified ejecta profiles described in Section 6.1 (full lines). The observed, extinction-corrected $L(t)$ and $T_{col}(t)$ are inferred from the data by assuming a specific extinction curve (MW, green data points, or SMC, cyan data points), and determining the absolute value of the extinction by requiring T_{col} inferred from the observations to agree with model prediction at $t \sim 2$ days. $E(B - V) = 0.625, 0.7$ and 0.8 are inferred for $R_* = 1, 3, 10 \times 10^{11}$ cm, respectively. Blue data points are obtained for (best-fit) extinction curves which are determined from the data itself, for the mixed He–C/O composition (see Figure 12).

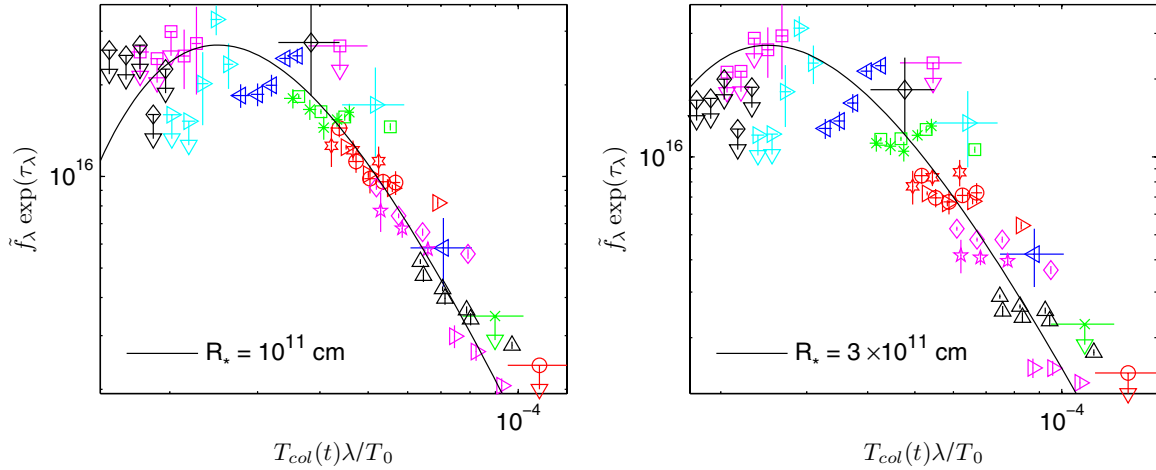(A color version of this figure is available in the online journal.)

Figure 11. Measured flux densities f_λ, corrected for extinction and scaled according to Equation (41) (using $D = 27$ Mpc and $T_0 = 1$ eV), compared with the model prediction of Equation (42) (solid line) for the mixed He–C/O composition models presented in Figure 10 with $R_* = 10^{11}$ cm and $R_* = 3 \times 10^{11}$ cm. Different symbols and colors show measurements at different bands: red circle—V, green cross—B, blue left triangle—U, cyan right triangle—$UVW1$, magenta square—$UVM1$, black diamond—$UVW2$, magenta pentagon—r, red hexagon—g, black triangle—i, magenta right triangle—z, (taken from Soderberg et al. 2008); black triangle—i', magenta diamond—r', red right triangle—B, green square—V (taken from Modjaz et al. 2009).

(A color version of this figure is available in the online journal.)

the spectral analysis of the observations at maximum light. As shown in Sections 2 and 3, E and M (mainly the ratio E/M) determine the normalization of the model luminosity, see Equations (25) and (29), but do not affect the time dependence of the luminosity, and T_{col} is nearly independent of E and M, see Equations (23) and (27). Since the conclusions drawn from the comparisons in fig. (10) are based on the time dependence of T_{col} and L, their validity is independent of the exact values chosen for E and M.

Figure 10 shows T_{col} and L for models with three progenitor radii, $R_* = 1, 3, 10 \times 10^{11}$ cm, and two compositions, He-dominated and mixed He–C/O composition with a He mass fraction $1 - Z = 0.3$. We show both the simple analytic approximations for L and T_{col} given in Section 3.1 (dashed curves), which are based on the self-similar ejecta profiles of Section 2.1, and L and T_{col} obtained solving Equations (21), (30), and (31) with the OP opacity tables for the modified ejecta profiles described in Section 6.1. Since models with larger initial radii predict higher T_{col}, the absolute extinction inferred for models with larger radii is larger, $E(B - V) = 0.625, 0.7$, and 0.8 for $R_* = 1, 3$, and 10×10^{11} cm, respectively. Once the absolute extinction is determined, from the comparison of observed and predicted T_{col} at $t \sim 2$ days, $T_{col}(t)$ and $L(t)$ are inferred from the observations using the two relative extinction curves (MW and SMC). In determining the observed T_{col} and L, the photometric measurements are converted into monochromatic fluxes at the effective wavelength of the broadband (BB) filters, and a BB temperature is determined by a least-squares fit to these fluxes. The resulting T_{col} and L are shown in Figure 10. The error bars represent the uncertainties obtained in the least-squares fits.

Examining Figure 10, we infer a small progenitor radius, $R_* \approx 10^{11}$ cm. Progenitors with larger radii require larger extinction to account for the observed flux distribution at $t = 2$ days, which in turn imply that the extinction corrected $L(t)$ decreases with time at $t < 2$ days, in contrast with the roughly time-independent L predicted by the models (see also Equations (25) and (29)), and that the extinction-corrected T_{col} decreases faster than predicted by the models for $t < 2$ days. This is due to the fact that at earlier times the flux is dominated by shorter wavelength bands, for which the extinction correction is

larger. Comparing model predictions and observations at $t > 2$ days, we find that a mixed He–C/O composition is preferred over an He-dominated one. The $Z = 0.7$ model presented provides a good fit to the data. We find that $Z \sim$ few tens of percent is required to fit the observations. Note, however, that the light curve at $t > 2$ days depends on the non-self-similar part of the density and pressure profiles of the ejecta, for which we have used the "harmonic-mean" approximation described in Section 6.1. As mentioned in Section 6.1, additional work, which is beyond the scope of this paper, is required in order to obtain a quantitative estimate of the accuracy of this approximation. We cannot rule out, therefore, the possibility that the observations may be explained with an He-dominated contribution and a density profile at large δ_m, that deviated from that given by the "harmonic-mean" approximation.

As explained in Section 4, R_* and the relative extinction between different wavelengths may be determined from the O/UV light curves by requiring that the light curves observed at different wavelengths should all be given, after scaling according to Equations (40) and (45), by a single function, given by Equation (42). In Figure 11, we compare the measured specific intensities, corrected for extinction and scaled according to Equations (40) and (45), with the model prediction, Equation (42). For the scaling, we have used $\{r_{ph}(t), T_{col}(t), T_{ph}(t)\}$ obtained for the mixed He–C/O composition models presented in Figure 10 with $R_* = 10^{11}$ cm and $R_* = 3 \times 10^{11}$ cm. The extinction τ_λ was obtained by requiring the scaled intensity to best fit that predicted by Equation (42) (taking into account all data points at $t < 4$ days). The resulting extinction curves are shown in Figure (12). As can been seen in the figure, the $R_* = 10^{11}$ cm model provides a much better description of the data than the $R_* = 3 \times 10^{11}$ cm model. The extinction curve is more compatible with an MW extinction than with SMC extinction. It differs from the MW curve at short wavelengths, showing no prominent graphite bump. This, as well as the values obtained for A_V and $E(B - V)$, $A_V = 2.39$, and $E(B - V) = 0.63$, is consistent with the extinction inferred in A. M. Soderberg et al. (2008, private communication).

The following point should be explained here. We have obtained the absolute values of the extinction by adopting some
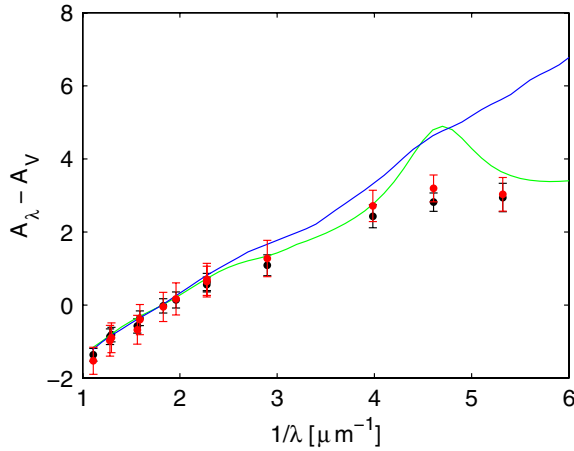
Figure 12. Comparison of the extinction curves inferred from the models described in Figure 11 (black and red points for $R_* = 10^{11}$ cm and $R_* = 3 \times 10^{11}$ cm, respectively) with $A_V = 2.21$ MW and $A_V = 2.16$ SMC extinction curves (Cardelli et al. 1989). We find $E(B-V) = 0.63, 0.70$ and $A_V = 2.39, 3.03$ for $R_* = 10^{11}$ cm and $R_* = 3 \times 10^{11}$ cm, respectively.
(A color version of this figure is available in the online journal.)

Figure 13. Comparison of the photospheric velocity of the best-fit model, in blue solid line, to results of other authors. Velocity from the He I $\lambda5876$ line is interpreted in green squares, and in green pentagon is the velocity from the analysis done via SYNOW to the "W" feature which later on vanishes both taken from Modjaz et al. (2009). In red circles the photospheric velocity measured from spectral modeling by Tanaka et al. (2009) is interpreted.
(A color version of this figure is available in the online journal.)

values for E and M. It is important to note, that, as explained in detail in Section 4, the relative extinction is independent of E and M, and may be inferred without making assumptions regarding their values. The model predicted temperature, T_{ph}, and T_{col}/T_{ph} are almost independent of E and M, and depend only on R_* (and on the composition). E and M determine the normalization of r_{ph}, $r_{ph} \propto E^{0.4}/M^{0.3}$ (see Equation (24)), but do not affect its time dependence. Thus, modifying E and M changes the scaled fluxes of Equation (41) by some multiplicative factor, which is wavelength independent. Thus, the ratios of the scaled fluxes at different wavelengths are independent of E and M, and so are the inferred relative extinctions. Using the relative extinction inferred from the data, and adopting some relation between the relative and absolute extinctions, which determines the absolution extinction (τ_λ), we may therefore constrain the $E^{0.4}/M^{0.3}$ ratio by comparing the predicted and measured (absolute) flux at some frequency. Using the inferred $E(B-V) = 0.63$ implies $A_V = 2.39$ for an MW extinction, for which we infer $E_{51}/(M/M_\odot) = 0.75$.

6.3. Comparison with Previous Work

Based on our analysis of the early UV/O emission of SN 2008D, we infer a small progenitor radius, $R_* \approx 10^{11}$ cm, an $E_{51}/(M/M_\odot) \approx 0.8$, a preference for a mixed He–C/O composition (with C/O mass fraction of tens of percent), $E(B-V) = 0.63$ and an extinction curve given by Figure 12. We compare below our conclusions to those of earlier analyses.

Explosion models for SN 2008D were consider by Mazzali et al. (2008) and by Tanaka et al. (2009). For E and M, Mazzali et al. (2008) infer $E_{51} \sim 6$ and $M \sim 7 M_\odot$, i.e., $E_{51}/(M/M_\odot) \sim 0.85$ while Tanaka et al. (2009) infer $E_{51} = 6 \pm 2.5$ and $M = 5.3 \pm 1 M_\odot$, and $E_{51}/(M/M_\odot)$ in the range $0.8 < E_{51}/(M/M_\odot) < 1.3$. These values are consistent with our inferred value of $E_{51}/(M/M_\odot) \approx 0.8$. The progenitor radius inferred from the (Tanaka et al. 2009) analysis is $0.9 \lesssim R_*/10^{11}$ cm $\lesssim 1.5$, also consistent with our inferred $R_* \approx 10^{11}$ cm.

In Figure 13, we compare the photospheric velocity obtained in our model with those obtained by Modjaz et al. (2009) and Tanaka et al. (2009) analyzing SN 2008D spectra. As
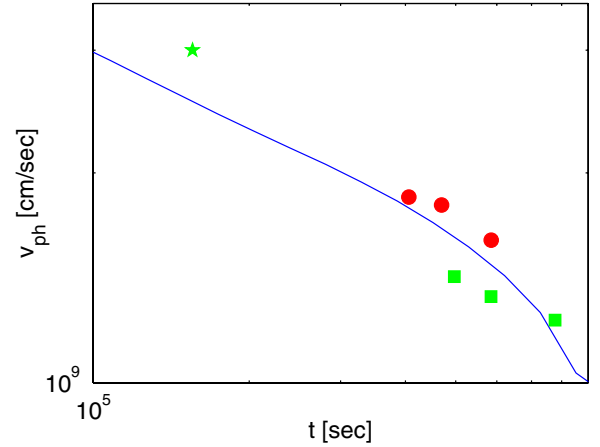
can be seen in the figure, our model predictions are in good agreement with the results inferred from the spectral analyses. We also note that Mazzali et al. (2008) infer, based on spectral analysis, that the mass of the ejecta shell moving at $> 0.1c$ is $\sim 0.03 M_\odot$, consistent with our model prediction of $\sim 0.02 M_\odot$ at this velocity.

Next, let us discuss our conclusion that the He envelope contains a significant (tens of %) C/O fraction. This conclusion is consistent with the results of Mazzali et al. (2008), who find a large fraction, $\sim 10\%$ of C at the fast $v > 25,000$ km s^{-1} He shells, rising to $\sim 30\%$ at the $v \simeq 20,000$ km s^{-1} shells (P. Mazzali 2010, private communication). Both Mazzali et al. (2008) and Tanaka et al. (2009) find a low, ~ 0.01, mass fraction of O at the fast shells.

Finally, we comment on the analysis of Chevalier & Fransson (2008), who find a large progenitor radius, $R_* \approx 10^{12}$ cm, based on both the X-ray and the UV/O emission. Chevalier & Fransson (2008) obtain $R_* \approx 10^{12}$ cm by interpreting the X-ray emission as thermal, $L_X = 4\pi R_*^2 \sigma T_X^4$, and adopting $T_X = 0.36$ keV. Their motivation for a thermal interpretation of the X-ray emission, despite the fact that the spectrum is non-thermal and extends beyond 10 keV, was that the non-thermal spectrum is difficult to explain theoretically. As explained in the Introduction, the non-thermal spectrum is a natural consequence of the physics of fast radiation mediated shocks (Katz et al. 2010). Thus, there is no motivation, and it is inappropriate, to infer R_* assuming thermal X-ray emission. Moreover, it should be kept in mind that the X-ray breakout may take place within the wind surrounding the progenitor, at a radius significantly larger than R_* (e.g., Waxman et al. 2007). The discrepancy between their large radius and our small radius inferred from the UV/O data is due to the fact that we take into account the modification of the opacity due to He recombination and the difference between color and effective temperatures. Since $R_* \propto \kappa$, neglecting the reduction of opacity due to HE recombination at $T = 1$ eV ($t \sim 1$ d) leads to a significant overestimate of the radius (compare Equations (33) and (34)), and neglecting the difference between color and effective temperatures leads to an additional overestimate of the radius, $R_* \propto T_{col}^4 = (T_{col}/T_{ph})^4 T_{ph}^4$ with $(T_{col}/T_{ph})^4 \approx 2$ (see Equation (34)).

7. CONCLUSION

We have presented a simple model for the early UV/O emission of core-collapse supernovae. The photospheric radius, $r_{ph}(t)$, and (effective) temperature, $T_{ph}(t)$, are given for H envelopes by Equations (12) and (13) in Section 2, and for He and mixed He–C/O envelopes (including pure C/O envelopes) by Equations (23)–(28) in Section 3.1. T_{ph} is determined by the composition and by the progenitor radius, R_*, and is nearly independent of the ejecta mass, M, and energy, E. M and E determine the normalization of $r_{ph}(t)$, but not its time dependence, $r_{ph} \propto E^{0.4}/M^{0.3}$. The bolometric luminosity predicted by the model is nearly time independent (for $T_{ph} > 1$ eV), see Equations (14), (15), (25), and (29). Both $r_{ph}(t)$ and $T_{ph}(t)$ are only weakly dependent on n, the exponent determining the dependence of the progenitor's density on the distance from the edge of the star, see Equation (1). A discussion of the deviation of the spectrum from a blackbody spectrum is given in Section 3.2, where we find that the ratio of color to effective temperature is approximately constant at early time, $T_{col}/T_{ph} \approx 1.2$ (see Figures 1–4).

For progenitor radii $R_* \lesssim 10^{12}$ cm, T_{ph} approaches 1 eV on day timescale. For He envelopes, significant recombination takes place at ~ 1 eV, leading to a significant reduction of the opacity, which, in turn, prevents T_{ph} from dropping significantly below 1 eV, since the photosphere penetrates (deeper) into the envelope up to the point where the temperature is high enough to sustain significant ionization (see Figure 2). Significant amounts of C/O in the envelope allow T_{ph} to drop below ~ 1 eV, since these atoms are partially ionized at lower temperatures as well (see Figure 4). Model predictions depend only weakly on the C:O ratio.

Since $T_{col}(t)$ is determined by the composition and by R_*, the progenitor radius may be inferred from the observed T_{col}. Equations (33)–(35) give R_* as a function of the observed T_{col} for H, He, and He–C/O envelopes. A few comments should be made at this point. For a space- and time-independent opacity, $R_* \propto \kappa T_{col}^4$ (see Equation (12)). In case κ varies with temperature and density, the appropriate value of κ, i.e., its value at the photosphere at the time T_{col} is measured, should be used. The fractional uncertainty in R_* is similar to the fractional uncertainty in κ. The strong dependence of R_* on T_{col} implies that relatively small uncertainties in the determination of T_{col} from the observations, or in its calculation in the model, lead to large uncertainties in the inferred R_*. Our approximate treatment of the deviation from blackbody spectrum due to photon diffusion implies that T_{col} is larger than T_{ph} by $\approx 20\%$. Estimating the uncertainty in the magnitude of this effect to be comparable to the magnitude of the effect implies a factor of ≈ 2 uncertainty in the inferred R_*. A more accurate estimate would require a more detailed treatment of photon transport (including the effects of effective line opacity enhancement due to the large velocity gradients, see Section 3.3).

Uncertainties in the observational determination of T_{col} are due to reddening. As explained in detail in Section 4, R_* and the relative extinction at different wavelengths may be inferred from the UV/O light curves. Scaling the observed light curves at different frequencies according to Equation (47), with $T_{col}(t)$ and $T_{ph}(t)$ obtained in a model with the correct value of R_*, should bring all the light curves to coincide, up to a factor $e^{-\tau_\lambda}$, where τ_λ is the extinction optical depth. The value of R_* may therefore be determined by requiring the ratios of scaled fluxes to be time independent, and the relative extinction between

two wavelengths may then be inferred from value of this ratio (see Equation (46)). For the case where the time dependence of the photospheric radius and of the photospheric and color temperatures are well approximated by power laws, which is a good approximation for the time dependence of r_{ph} in general and for the time dependence of T_{col} and T_{ph} for $T_{ph} > 1$ eV, the relative extinction may be inferred independently of R_*, from the ratio of the fluxes scaled according to Equation (45).

In Section 5, we have compared our model predictions to observations of the early UV/O emission available for two SNe (SN1987A and SNLS−04D2dc), arising from RSG and BSG progenitors, and to detailed numerical (radiation transport-hydrodynamics) simulations, that were constructed to reproduce these observations (Blinnikov et al. 2000; Gezari et al. 2008). We have shown that our simple model may explain the observations. We find, however, that our predicted luminosity is ≈ 2 times larger than that obtained (for similar progenitor and explosion parameters) by the detailed numerical simulations. In the case of the BSG SN, this discrepancy is probably due to differences in the opacity tables we use and those used in the simulations ($L \propto 1/\kappa$, see Section 5.1). In the case of the RSG SN, the discrepancy is due to the fact that our model predicts a somewhat ($\sim 40\%$) larger velocity for the fast outer shells, and hence a larger photospheric radius than that obtained in the numerical simulation. Since the details of the explosion model of Gezari et al. (2008) are not given in their paper, it is difficult to determine the source of this discrepancy. In a subsequent publication (I. Rabinak et al. 2011, in preparation), we will examine the accuracy of the approximate ejecta density and velocity profiles described in Section 2.1 for a wide range of progenitor models.

In Section 6, we have used our model to analyze the early UV/O measurements of SN 2008D. For this explosion, we infer a small progenitor radius, $R_* \approx 10^{11}$ cm, an $E_{51}/(M/M_\odot) \approx 0.8$, a preference for a mixed He–C/O composition (with C/O mass fraction of tens of percent), $E(B - V) = 0.63$, and an extinction curve given by Figure 12. Our results are consistent (see discussion in Section 6.3) with the E/M values inferred from modeling the light curve and spectra at maximum light (Mazzali et al. 2008; Tanaka et al. 2009), with the R_* range obtained in the stellar evolution models described in Tanaka et al. (2009), and with the extinction inferred from the analyses of spectra at maximum light (e.g., Soderberg et al. 2008). The photospheric velocity predicted by our model is consistent with the velocities inferred from spectral analyses (Mazzali et al. 2008; Modjaz et al. 2009; Tanaka et al. 2009), see Figure 13.

Our conclusion that the He envelope contains a significant (tens of percent) C/O fraction is not as robust as the other conclusions, since it relies on observations at $t > 2$ d, where the emission is dominated by shells that were initially located at distances from the edge of the star for which the asymptotic (self-similar) description of the density, Equation (1), does not hold (see detailed discussion in Section 6.2). In order to describe the light curve at $t > 2$ d, we have used the approximation described in Section 6.1 for the density and pressure profiles of the ejecta. Additional work, which is beyond the scope of this paper, is required in order to obtain a quantitative estimate of the accuracy of this approximation. We cannot rule out, therefore, the possibility that the observations may be explained with a He-dominated composition and a density profile that deviates from the approximation used. Nevertheless, our conclusion is consistent with the analysis of Mazzali et al. (2008), who find a large fraction, $\sim 10\%$ of C at the fast $v > 25,000$ km s^{-1}

He shells, rising to ~30% at the $v \simeq 20{,}000$ km s^{-1} shells (P. Mazzali 2010, private communication). Both Mazzali et al. and Tanaka et al. (2009) find a low, ~0.01, mass fraction of O at the fastest shells.

The comparison of our analysis of the early emission of SN 2008D with the analyses of the light curve and spectra at maximum light indicates that a combined model, describing both the early emission from the expanding and cooling envelope and the emission at maximum light, which is driven by radioactive decay, will provide much better constraints on the progenitor and explosion parameters than those that may be obtained by analyzing either of the two separately.

REFERENCES

Band, D. L., et al. 2008, ApJ, 673, 1225
Bernstein, I. B., & Book, D. L. 1980, ApJ, 240, 223
Blinnikov, S. I., Eastman, R., Bartunov, O. S., Popolitov, V. A., & Woosley, S. E. 1998, ApJ, 496, 454
Blinnikov, S., Lundqvist, P., Bartunov, O., Nomoto, K., & Iwamoto, K. 2000, ApJ, 532, 1132
Blinnikov, S. I., Nadyozhin, D. K., Woosley, S. E., & Sorokina, E. I. 2002, in Proc. of 11th Workshop on Nuclear Astrophysics, ed. W. Hillebrandt & E. Müller (München: Max-Planck-Institut Für Astrophysik), 144
Calzavara, A. J., & Matzner, C. D. 2004, MNRAS, 351, 694
Campana, S., et al. 2006, Nature, 442, 1008
Cardelli, J. A., Clayton, G. C., & Mathis, J. S. 1989, ApJ, 345, 245
Castor, J. I. 2004, Radiation Hydrodynamics (Cambridge: Cambridge Univ. Press)
Chandrasekhar, S. (ed.) 1939, in An Introduction to the Study of Stellar Structure (Chicago, IL: Univ. of Chicago)
Chevalier, R. A. 1992, ApJ, 394, 599
Chevalier, R. A., & Fransson, C. 2008, ApJ, 683, L135
Chevalier, R. A., & Soker, N. 1989, ApJ, 341, 867
Colgate, S. A. 1974, ApJ, 187, 333
Crowther, P. A. 2007, ARA&A, 45, 177
Dessart, L., & Hillier, D. J. 2005, A&A, 437, 667
Eastman, R. G., & Pinto, P. A. 1993, ApJ, 412, 731
Ensman, L., & Burrows, A. 1992, ApJ, 393, 742
Falk, S. W. 1978, ApJ, 225, L133

Fan, Y., Piran, T., & Xu, D. 2006, J. Cosmol. Astropart. Phys., 9, 13
Friend, D. B., & Castor, J. I. 1983, ApJ, 272, 259
Gaffet, B. 1984, A&A, 135, 94
Gandel'Man, G. M., & Frank-Kamenetskii, D. A. 1956, Sov. Phys. Dokl., 1, 223
Gezari, S., et al. 2008, ApJ, 683, L131
Ghisellini, G., Ghirlanda, G., & Tavecchio, F. 2007, MNRAS, 382, L77
Grindlay, J. E., Craig, W. W., Gehrels, N. A., Harrison, F. A., & Hong, J. 2003, Proc. SPIE, 4851, 331
Hauschildt, P. H., & Ensman, L. M. 1994, ApJ, 424, 905
Karp, A. H., Lasher, G., Chan, K. L., & Salpeter, E. E. 1977, ApJ, 214, 161
Katz, B., Budnik, R., & Waxman, E. 2010, ApJ, 716, 781
Klein, R. I., & Chevalier, R. A. 1978, ApJ, 223, L109
Law, N. M., et al. 2009, PASP, 121, 1395
Li, L. 2007, MNRAS, 375, 240
Li, L. 2008, MNRAS, 388, 603
Maeda, K., et al. 2007, ApJ, 658, L5
Malesani, D., et al. 2009, ApJ, 692, L84
Matsuoka, M., et al. 1997, Proc. SPIE, 3114, 414
Matzner, C. D., & McKee, C. F. 1999, ApJ, 510, 379
Mazzali, P. A., et al. 2006, Nature, 442, 1018
Mazzali, P. A., et al. 2008, Science, 321, 1185
Meynet, G., & Maeder, A. 2003, A&A, 404, 975
Mihalas, D., & Mihalas, B. W. 1984, in Foundations of Radiation Hydrodynamics, ed. B. W. Mihalas & D. Mihalas (New York, NY: Oxford Univ. Press)
Modjaz, M., et al. 2006, ApJ, 645, L21
Modjaz, M., et al. 2009, ApJ, 702, 226
Nomoto, K. I., Iwamoto, K., & Suzuki, T. 1995, Phys. Rep., 256, 173
Pian, E., et al. 2006, Nature, 442, 1011
Quimby, R. M. 2006, PhD thesis, University of Texas, TX, USA
Sakurai, A. 1960, Commun. Pure Appl. Math., 13, 353
Schawinski, K., et al. 2008, Science, 321, 223
Seaton, M. J. 2005, MNRAS, 362, L1
Sedov, L. I. 1959, in Similarity and Dimensional Methods in Mechanics, ed. L. I. Sedov (New York, NY: Academic Press)
Soderberg, A. M., et al. 2006, Nature, 442, 1014
Soderberg, A. M., et al. 2008, Nature, 453, 469
Tanaka, M., et al. 2009, ApJ, 692, 1131
Taylor, G. 1950, Proc. R. Soc. A, 201, 175
Von Neumann, J. 1947, in Los Alamos Sci. Lab. Tech. Series, Vol. 7, Blast Waves, ed. L. I. Sedov (Los Alamos, NM)
Wagoner, R. V., Perez, C. A., & Vasu, M. 1991, ApJ, 377, 639
Waxman, E., Meszaros, P., & Campana, S. 2007, ApJ, 667, 351
Weaver, T. A., Zimmerman, G. B., & Woosley, S. E. 1978, ApJ, 225, 1021
Woosley, S. E., Langer, N., & Weaver, T. A. 1993, ApJ, 411, 823
Woosley, S. E., & Weaver, T. A. 1986, ARA&A, 24, 205